

Spin-polarized scanning tunneling microscopy study of
the Fe(001)-p(1×1)O surface and antiferromagnetic Mn
films on Fe(001)-p(1×1)O and Cu₃Au(100)

Dissertation

Zur Erlangung des akademischen Grades

Doctor rerum naturalium (Dr. rer. nat.)

vorgelegt der

die Naturwissenschaftliche Fakultät II

Institut für Physik

Der Martin-Luther-Universität Halle-Wittenberg

von Hern Achiri Celestine Tange

geboren am 10.12.1975 in Victoria, Cameroon

Gutachter:

1. Prof. Dr. Jürgen Kirschner
2. Prof. Dr. em. Henning Neddermeyer
3. Prof. Dr. Markus Morgenstern

Halle (Saale), 2009

verteidigt am 14.04.2009

Abstract

The first part of this thesis explores the adsorption of oxygen on Fe(001) which gives an ordered $p(1\times 1)$ surface studied by spin-polarized scanning tunneling microscopy (Sp-STM) and spectroscopy (Sp-STs) as well as the effect of the oxygen overlayer on the growth and magnetic structure of Mn films on Fe(001). The Sp-STM used in the experiments operates in the differential magnetic mode using a soft ferromagnetic ring as the probe electrode, effectively separating the topographic and spin information. The atomic registry of the Fe(001)- $p(1\times 1)$ O surface was confirmed in real space from atomically resolved STM data. Sp-STs measurements show an oxygen induced feature in the local density of states below the Fermi level, the origin of which is discussed based on first principle calculations. The oxygen overlayer is found to play a surfactant role on the growth of thin Mn films on Fe(001)- $p(1\times 1)$ O, improving the layer-by-layer growth. Sp-STM measurements reveal that the Mn films show uncompensated layerwise antiferromagnetic order similar to Mn films grown on the clean Fe(001) surface but with an enhanced tunneling magnetoresistance effect compared to the latter.

In the second part of this thesis, the magnetic properties of face-centered tetragonal (fct) Mn films deposited on $\text{Cu}_3\text{Au}(100)$ was studied using Sp-STM. Previous experiments had shown significant exchange bias in the system Fe/Mn/ $\text{Cu}_3\text{Au}(100)$, indicating the antiferromagnetism of Mn/ $\text{Cu}_3\text{Au}(100)$. Here it is shown directly using Sp-STM that fct Mn on $\text{Cu}_3\text{Au}(100)$ has an uncompensated antiferromagnetic spin structure.

Kurzfassung

Der erste Teil dieser Arbeit beschäftigt sich mit der Adsorption von Sauerstoff auf einer Fe(001) oberfläche, welches zu einer $p(1 \times 1)$ Oberfläche führt, die mittels spin-aufgelöster Rastertunnelmikroskopie (Sp-STM) und Spektroskopie (Sp-STs) untersucht wird. Ebenso wird der Effekt einer Sauerstofflage auf das Wachstum und den Magnetischen Eigenschaften von Mn Filmen auf Fe(001) betrachtet. Das verwendete Sp-STM arbeitet im differentiell magnetischen Modus, wobei ein ferromagnetisch weicher Ring als Probenelektrode verwendet wird, der es ermöglicht, die Topologie- und die Spininformationen zu separieren. Die bekannte atomare Struktur der Fe(001)- $p(1 \times 1)$ O Oberfläche wurde im Realraum von atomar aufgelösten STM Daten bestätigt. Sp-STs Messungen zeigen eine durch Sauerstoff hervorgerufene Besonderheit in der lokalen Zustandsdichte, deren Herkunft mittels „*ab initio*“ Rechnungen diskutiert wird. Wie sich zeigt, spielt die Sauerstofflage eine benetzende Rolle beim Wachstum von dünnen Mn Filmen auf Fe(001)- $p(1 \times 1)$ O, wobei das lagenweise Wachstum verbessert wird. Sp-STM Messungen zeigen, dass die Mn Filme eine unkompenzierte lagenweise antiferromagnetische Ordnung aufweisen, ganz ähnlich zu Mn Filmen, die auf einer reinen Fe(001) Oberfläche gewachsen sind, jedoch im Vergleich zu diesen mit vergrößertem Tunnelwiderstandseffekt.

Im zweiten Teil dieser Arbeit werden magnetische Eigenschaften der „face-centered tetragonal (fct)“ von auf Mn Filmen auf $\text{Cu}_3\text{Au}(100)$ mittels der Sp-STM untersucht. Frühere Experimente am System Fe/Mn/ $\text{Cu}_3\text{Au}(100)$ haben einen signifikanten Austausch-Verschiebnungs-Effekt gezeigt, die auf Antiferromagnetismus von Mn/ $\text{Cu}_3\text{Au}(100)$ schließen lassen. Hier wird direkt gezeigt, dass die fct von Mn/ $\text{Cu}_3\text{Au}(100)$ eine unkompenzierte antiferromagnetische Spinstruktur aufweist.

Table of Contents

1	Introduction	1
2	Theoretical Background	5
2.1	Magnetism in reduced dimensions: From bulk to surfaces and thin films	5
2.2	Effect of chemisorption on magnetism	8
2.3	Quantum mechanical tunneling and scanning tunneling microscopy.....	8
2.3.1	Spin dependent tunneling	12
3	Experimental Setup	18
3.1	The ultrahigh vacuum chamber	18
3.2	The Spin-polarized STM setup.....	21
3.3	In-situ sample preparation.....	25
4	Oxygen on Fe(001)	27
4.1	Preparation of Fe(001)-p(1×1)O.....	27
4.2	The Fe(001)-p(1×1)O Surface: Structure and Magnetism.....	30
4.3	Sp-STs on Fe(001)-p(1×1)O.....	34
4.4	Discussion.....	36
4.4.1	Identifying the atomic registry of Fe(001)-p(1×)O from STM.....	36
4.4.2	Spin density from the Fe(001)-p(1×1)O surface.....	37
4.4.3	Spin-resolved density of states of Fe(001)-p(1×1)O.....	39
5	Mn Films on Fe(001)-p(1×1)O	46
5.1	Properties of Mn on Fe(001).....	46
5.2	Growth of Mn on Fe(001)-p(1×1)O.....	47
5.3	Magnetic structure of Mn films on Fe(001)-p(1×1)O.....	51
5.3.1	Topologically-induced Magnetic Frustrations.....	52
5.3.2	Voltage dependence of the spin contrast.....	56

6 Mn on Cu₃Au(100)	60
6.1 Growth of Mn on Cu ₃ Au(100).....	60
6.1.1 Surface structure of Mn films on Cu ₃ Au(100).....	62
6.2 Magnetic order of Mn films on Cu ₃ Au(100).....	63
6.2.1 p-(2×2) Superstructure.....	67
7 Conclusion	69

Chapter 1

Introduction

Our high-tech world is driven by its desire for even smaller and cheaper electronic devices with more and more functionality. As the size of these devices continuously shrinks the surface to volume ratio of atoms increases significantly and quantum size effects become more evident. Understanding the novel properties that arise as a result of this reduced dimensionality is of fundamental importance. Magnetic nanostructures play an important role in modern data storage devices. Future storage devices will utilize the spin of the electron instead of its charge for data storage; hence understanding the spin structure of magnetic materials at the nanoscale and especially in real space is of interest. By imaging magnetic structures in real space, there is the additional advantage of access to non periodic and more localized magnetic structures compared to methods that operate in reciprocal space like neutron diffraction [1].

Most conventional magnetic imaging techniques though useful in their own right, are limited in terms of lateral resolution. The magnetic force microscope (MFM) which maps the magnetostatic interaction between a magnetic tip and the stray field from a sample as a function of the lateral position of the tip, can only achieve a lateral resolution between 20 nm to 100 nm [2, 3]. Magneto-optic Kerr microscopy analyzes changes in the polarization of light upon reflection from a sample surface to map of the local magnetization of the sample surface [4]. The resolution in this case is limited by the wavelength of the light which is usually a few hundred nanometers. Electron microscopes can also give information about the magnetization configuration in a sample if the spin of the electron is considered. Scanning electron microscopy with polarization analysis (SEMPA), for instance measures the spin polarization of the low energy secondary electrons emitted from

a sample while a focused high energy (about 10 keV) electron beam is scanned over the sample surface [5]. SEMPA can achieve resolutions up to a few tens of nanometers. In the case of alloyed films and multilayered structures, the photoemission electron microscope (PEEM) exploits the different absorption energies of core level electrons to map the magnetization configuration in an element specific way [6]. The ultimate magnetic imaging tool should be able to image individual atomic moments, since these constitute the basic building units of magnetic materials. The invention of the scanning tunneling microscope (STM) by Binnig and Rohrer [7, 8] with its atomic resolution capabilities, paved the way for the spin-polarized scanning tunneling microscope (Sp-STM) [9, 10]. It combines the high lateral resolution of the STM with spin sensitivity to resolve complex spin structures at the atomic scale.

Magnetic thin films and surfaces, whose properties are known to deviate considerably from the corresponding bulk properties, are model systems to investigate magnetism in reduced dimensions. The modification of the electronic structure at the surface is of primary importance to surface magnetism. Due to the existence of surface states and the different environment relative to the bulk (broken translational symmetry and reduced atomic coordination), the magnetic moments of surface atoms in a magnetic material are greatly enhanced [11, 12]. In the case of body-centered cubic (bcc) Fe(001), for example, there is an enhancement of the surface magnetic moments by more than 30% with respect to the bulk value [13]. Of particular interest is the effect of foreign atoms or impurities adsorbed on the surface. When the substrate is magnetic, additional issues involving the role electron spin polarization plays in all of the physical processes can also be addressed. The presence of adsorbates is known to affect the magnetic moments of atoms at the surface of ferromagnetic materials. For adsorbed oxygen on Fe(001), theoretical calculations [14, 15] and experiment [16, 17] showed an enhancement of the magnetic moment of surface Fe atoms.

The magnetic properties of ultrathin films depend on their atomic scale structure, for example, the presence of atomic steps can cause a rotation of the preferred orientation of atomic spins [18]. The availability of modern *in situ* growth techniques like molecular beam epitaxy (MBE) in recent years, has greatly

improved the preparation of almost ideal film structures and facilitated the understanding of the correlation between the structure and magnetic properties of ultrathin magnetic films [18, 19]. Of particular interest for magnetic devices is the case of an antiferromagnet in contact with a ferromagnet. The antiferromagnet acts as a reference to pin the magnetization of the ferromagnet across the interface [20] but the physical origin of the coupling between the ferromagnet and the antiferromagnet at the interface is not yet fully understood. Such structures are used in the read heads of hard drives. Here it is shown that the growth and magnetic properties of the antiferromagnetic film is significantly improved when stabilized on an oxygen-covered ferromagnetic substrate.

This thesis is organized as follows: Chapter 2 gives a brief overview of magnetism in reduced dimensions and introduces the various operation modes of the Sp-STM. In Chapter 3 a brief description of the experimental setup is given with special emphasis on how to realize spin-polarized STM measurements with a ferromagnetic ring electrode. The preparation and characterization of the Fe(001)-p(1×1)O system is discussed in Chapter 4. The surface atomic structure from STM is found to agree well with Low Energy Electron Diffraction (LEED) measurements and first principle calculations. Scanning tunneling spectroscopy (STS) measurements reveal an oxygen-induced feature in the differential conductance spectrum below the Fermi energy, the origin of which is discussed based on *ab initio* calculations using the Korringa-Kohn-Rostoker (KKR) Green function method. In Chapter 5 the growth, surface structure and magnetism of Mn on Fe(001)-p(1×1)O is discussed. The oxygen is found to play a surfactant role improving the layer-by-layer growth of the Mn films in comparison to those grown on clean Fe(001). The films show layerwise antiferromagnetic order with an enhanced tunneling magnetoresistance (TMR) compared to Mn films on clean Fe. Chapter 6 presents the results of the magnetic structure of face-centered tetragonal (fct) γ -Mn stabilized on Cu₃Au(100) and finally a brief summary and conclusion is given in Chapter 7.

Chapter 2

Theoretical Background

2.1 Magnetism in reduced dimensions: From bulk to surfaces and thin films

The phenomenon of magnetism is a consequence of the fact that electrons in atoms have spin and obey the exclusion principle. Therefore, depending on its electronic structure an atom may possess a magnetic moment. In a solid these atomic moments can spontaneously order below a critical temperature resulting in ferromagnetism, when the moments are aligned parallel or antiferromagnetism when the moments are aligned antiparallel. For ferromagnets, this critical temperature is called the Curie temperature, T_C , while for antiferromagnets it is the Néel temperature, T_N . This spontaneous ordering of the atomic moments is a result of the exchange interaction which is a consequence of the exclusion principle and the electrostatic Coulomb interaction between electrons. Due to the exclusion principle, two electrons on the same atom prefer to have the same spins since they cannot occupy the same orbital state and so cannot come too close to each other. Thus their electrostatic interaction energy is reduced. The Heisenberg model [18] can be used to describe the exchange interaction between localized moments. In this model the Hamiltonian can be expressed as

$$H = -\frac{1}{2} \sum_{i,j \neq i} J_{ij} \vec{S}_i \cdot \vec{S}_j \quad (2.1)$$

where $\vec{S}_{i(j)}$ is the total spin moment of the atom at position i (j) and J_{ij} is the exchange coupling constant. If J_{ij} is positive the energy is lower when the spins are in the same spin state, the spins align parallel and ferromagnetic order is

preferred. When J_{ij} is negative the energy is lower if the two spins are in different spin states. In this case, spins align antiparallel such that the total magnetic moment vanishes and antiferromagnetic order is preferred.

In the 3d metals, where the electrons are arranged in bands, their magnetic properties can be explained better by the band model introduced by Stoner [21].

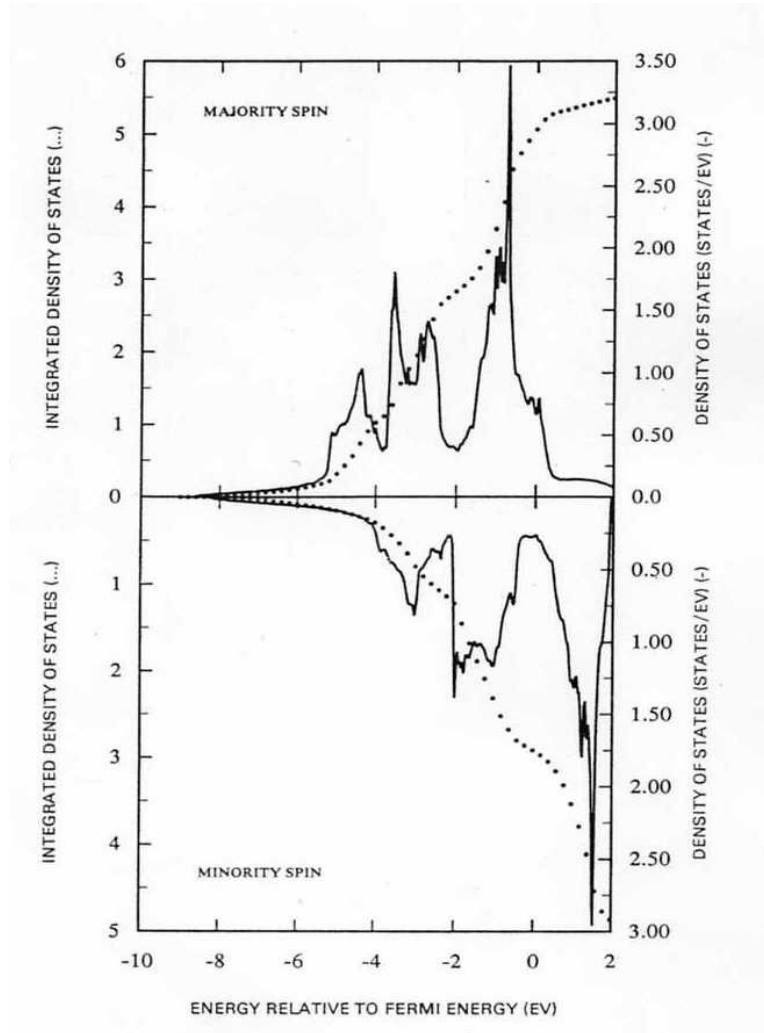


Fig. 2.1: Calculated density of states (DOS) of bcc Fe taken from ref [22]. The DOS of majority electrons is plotted upwards while that for minority electrons is plotted downwards. States for positive energies are unoccupied while states for negative energies are occupied. The energy scale is given relative to the Fermi energy E_F . The dotted curves show the integrated DOS.

In a partially filled band, it is possible to have an imbalance of spins due to the exchange interaction which tends to favor parallel alignment of spins. This leads to an uneven distribution of spin-up and spin-down electrons and a net magnetic moment. The d-band is then said to be exchange split into spin-up and spin-down sub-bands. The DOS of bulk iron is shown in Fig. 2.1. One can see clearly that the DOS is not symmetric for spin-up and spin-down electrons (as in nonmagnetic metals). This asymmetry causes a spin polarization of the conduction electrons and consequently a difference in the tunneling probability for spin-up and spin-down electrons close to the Fermi level, as will be discussed below. The DOS at the Fermi energy E_F is dominated by spin up electrons (which are referred to as majority) and as such the spin polarization of bulk bcc iron has a positive value at E_F . For bulk Co and Ni the spin polarization is negative since the DOS at E_F is dominated by electrons of minority character.

As one moves from the bulk to the surface, symmetry breaking and the reduced coordination lead to a narrowing of metallic bands and the creation of surface states that alter the DOS at the Fermi level. One consequence is an enhancement of the surface magnetic moments with respect to the bulk. The enhancement for a given bulk material is larger if the number of nearest neighbors is smaller. Thus the enhancement for a bcc (100) surface is larger than the corresponding (110) surface. The change in the DOS at the Fermi level on the surface may also have an effect on the sign of the spin polarization at this level, as in bcc Fe where the spin polarization becomes negative at the surface [23].

Similar to the surface enhancement of the magnetic moment for the 3d metals, there is a much larger enhancement in the monolayer regime. If one considers the single monolayer as a two dimensional (2D) structure, then it is obvious that the reduced coordination number of nearest neighbors causes a much narrower d-band in 2D compared to 3D.

Transition metal monolayers grown on noble metal substrates form approximate experimental realization of 2D itinerant magnets [24]. Since the noble metal d-band is well below the Fermi energy this results in small d-d hybridization between the film and substrate. Thus it is possible to have ferromagnetism in 3d and 4d metals in the monolayer regime when stabilized on noble metal substrates.

2.2 Effect of chemisorption on magnetism

Scientific interest in atomic and molecular processes at metal surfaces is driven not only by the broad technological implications of surface chemical effects, but also by the opportunities chemisorbed atoms provide for exploring fundamental physical processes at surfaces [25]. Chemisorption is the adsorption of a particle at the surface of a solid with the formation of a chemical bond with one or more surface atoms. As a molecule approaches a surface, it can directly adsorb as a molecule or it can undergo dissociative adsorption, whereby it breaks down into single atoms when hitting the surface. The presence of the adsorbed species causes modifications to the electronic structure as well as magnetism of the surface (sometimes leading to magnetically “dead” layers [26]). The adsorbate itself is modified due to interaction with the substrate. The adsorption of nonmagnetic atoms on magnetic surfaces may lead to an induced magnetic moment on the adsorbate [27] and in some cases an enhancement of the Curie temperature of the substrate [28]. In Chapter four the effect of oxygen adsorption on the magnetism of bcc Fe(001) will be discussed in more detail.

2.3 Quantum mechanical tunneling and scanning tunneling microscopy

In classical mechanics, an electron cannot overcome a potential energy barrier greater than its kinetic energy. It is only reflected from such a barrier. In quantum mechanics, where the wave nature of the electron is exploited, it has a finite probability of penetrating or tunneling through the barrier. The concept of tunneling had been put forward since the 1920s, during heydays of quantum mechanics and was used to explain mechanisms like α -particle decay [29] and field emission of electrons from metal surfaces [30]. The transmission probability for an electron with kinetic energy E through a finite barrier of potential height V ($V > E$) and width d can be found by solving the Schrödinger equation

$$\left[-\frac{\hbar^2}{2m} \frac{\partial^2}{\partial x^2} + V(x) \right] \Psi(x) = E\Psi(x) \quad (2.1)$$

For the simple case of a rectangular barrier and one dimensional tunneling considered above, the wavefunction within the barrier has the form

$$\Psi(x) = Ae^{-\kappa x} \quad (2.2)$$

where A is a constant and the wave vector $\kappa = \sqrt{2m(V - E)} / \hbar$. The barrier transmission coefficient (ratio of incident and transmitted current densities) can be expressed in the form

$$T \propto e^{-2\kappa d} \quad (2.3)$$

From equation (2.3) one sees that the transmission probability decays exponentially with the barrier width (d). By applying a voltage across the barrier, a net tunneling current can be detected which also decays exponentially with the barrier width. For typical barrier heights given by the work function of metals, the tunneling current changes by one order of magnitude if the barrier width changes by just 1 Å. It is this high sensitivity of the tunneling current on the barrier width that was applied by Binnig and Rohrer [7, 31] to operate the first scanning tunneling microscope (STM).

In a metal the electrons need to overcome the work function in order to escape into the vacuum. The Fermi level is below the vacuum level by an amount equal to the work function. When two metals with work functions Φ_t and Φ_s are placed within a few angstroms of each other, electrons can tunnel across the gap separating the metals from occupied states in one to unoccupied states in the other. The situation is shown schematically in Fig. 2.2.

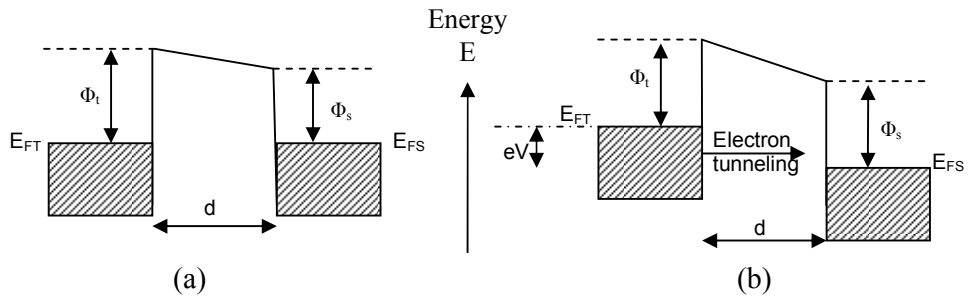


Fig. 2.2: Energy level diagram for tunneling between two metals separated by a tunneling barrier of width d for (a) the equilibrium state and (b) after a voltage V is applied. The shaded regions indicate occupied states up to the respective Fermi energies E_{FT} and E_{FS} .

In the equilibrium state, the net tunneling current is zero (as the Fermi levels are the same and the amount of tunneling is equal in both directions). When a small positive voltage V is applied to the left metal, the effect is to raise its Fermi level with respect to the other, i.e. the electronic states of the left metal are shifted by an amount eV . There will be a net tunneling current from the occupied states of the left metal to the unoccupied states of the right one. A reverse current arises if the sign of the applied voltage is reversed. Thus the states contributing to the tunneling process depend on the applied voltage. In a STM, the left metal is replaced with a sharp metal tip that can be scanned laterally over a sample surface and controlled vertically in a way that the tip-to-sample distance can be varied in order to keep the tunneling current constant. In this mode of operation (the constant current mode), the vertical position of the tip as a function of the lateral position on the surface is measured to obtain a contour map which reflects the topography of the surface.

Before the advent of the STM, Bardeen [32] gave a generalized description of a tunneling junction in three dimensions. In his treatment the two electrodes are considered as weakly coupled and the tunneling current is calculated by evaluating the tunnel matrix elements $M_{\mu\nu}$ from an initial state μ to a final state ν .

$$M_{\mu\nu} = \frac{\hbar}{2m} \int_S d\bar{S} (\psi_\mu^* \bar{\nabla} \psi_\nu - \psi_\nu \bar{\nabla} \psi_\mu^*) \quad (2.4)$$

where ψ_μ and ψ_ν are the wavefunctions of the initial and final states, respectively, and the integral is taken over a surface S lying within the vacuum. From the transition rate $|M_{\mu\nu}|^2$, the net tunneling current is calculated by summing over all states responsible for tunneling. Thus the tunneling current has the form

$$I = \frac{2\pi e}{\hbar} \sum_{\mu\nu} |M_{\mu\nu}|^2 \delta(E_\mu - E_\nu) (f(E_\mu) - f(E_\nu + eV)) \quad (2.5)$$

where E_μ and E_ν are the energies of the states with wavefunctions ψ_μ and ψ_ν , V the applied voltage and $f(E)$ the Fermi-Dirac function, which takes into account the fact that tunneling occurs from occupied to unoccupied states. The δ -function ensures energy conservation in the case of elastic tunneling.

To extend this generic case to the specific case of the STM, one needs a full knowledge of the electronic structure of both the tip and the sample. In their approximation, Tersoff and Hamann [33, 34] modeled the tip with a spherical wave

with constant electronic structure and considered a wave function for the sample that decays exponentially into the vacuum while propagating freely along the surface plane. Using this approximation and in the limit of small voltages and temperatures, they showed that the tunneling current in equation (2.5) can be reduced to the form

$$I \propto \sum_s |\psi_s(\vec{r}_o)|^2 \delta(E_s - E_F) \quad (2.6)$$

where $|\psi_s(\vec{r}_o)|^2$ is the amplitude of the sample wavefunction at the position of the tip \vec{r}_o , E_s the energy of the unperturbed wavefunction of the sample and E_F the Fermi energy. Equation (2.6) implies that the tunneling current is proportional to the sample surface local density of states (LDOS) at E_F at the position of the probe tip, which represents the charge density from states at E_F . Therefore, what we see in the STM image is simply a contour map of the constant surface LDOS of the sample. Within this model, since in the direction normal to the surface the sample wavefunction decays exponentially then $|\psi_s(\vec{r})|^2 \propto e^{-2\kappa(d+R)}$, where R is the radius of curvature of the tip and d the distance of closest approach from the sample surface. Therefore, $I \propto e^{-2\kappa d}$ as expected i.e. a change of the tip-to-sample distance by 1 Å results in a change of the tunneling current by a factor of 10.

In addition to mapping the topography of the surface, the STM can also be used to study (locally) the electronic properties of the sample surface at any given energy. This mode of operation is called scanning tunneling spectroscopy (STS) and has been extensively used to study the electronic properties of semiconductor surfaces. When a positive voltage is applied to the sample, electrons tunnel from the occupied states of the tip to the unoccupied states of the sample, while for a negative sample bias, electrons tunnel from the occupied states of the sample to the unoccupied states of the tip. This means one can effectively choose the states involved in the tunneling by simply changing the applied voltage. For small biases, the tunneling current can be written as a convolution of the DOS of the sample ρ_s and tip ρ_t :

$$I \propto \int_0^{eV} \rho_s(\vec{r}, E) \rho_t(E - eV) dE \quad (2.7)$$

Assuming that the tip has a constant DOS in the energy range of the measurement;

$$\frac{dI}{dV} \propto \rho_s(\vec{r}, eV) \quad (2.8)$$

Equation (2.8) shows that the tunneling conductance is directly proportional to the sample LDOS. In a STS experiment, the tip is scanned over the sample surface and at each spatial position the tip-to-sample distance is fixed for a short time while the voltage is ramped to obtain $I(V)$ data, which can be numerically differentiated to get dI/dV . An alternative way is to obtain dI/dV directly via a modulation technique. This involves superimposing a sinusoidal modulation voltage on the constant d.c. voltage at a frequency higher than the cut-off frequency of the STM feedback loop. The signal of the resulting tunneling current modulation in phase with the applied a.c. voltage can be detected with a lock-in amplifier and corresponds to dI/dV .

2.3.1 Spin-dependent tunneling

Spin generally refers to the angular momentum intrinsic to a body. According to quantum mechanics, angular momentum is quantized in units of $S = \hbar\sqrt{s(s+1)}$, ($s = 0, \frac{1}{2}, 1, \frac{3}{2}, \dots$). Electrons are spin-1/2 particles and so there are only two possible components of their angular momentum in any given direction. For example, in the z-direction with $s_z = \pm 1/2$, the two possible states are referred to as spin-up and spin-down, respectively. As discussed before, the band structure of a magnetic material is exchange split such that the occupations for spin-up and spin-down electrons are unequal. If two such materials are brought close to each other like in the normal STM geometry, one needs to consider the effect of the spin of the electrons on the tunneling current between the materials. This situation was first treated by Jullière [35] who found that the magnitude of the tunneling current depends on the magnetization of the two electrodes. For two ferromagnetic electrodes separated by an insulating layer, the tunneling current is higher when their magnetization directions are aligned parallel and lower for an antiparallel alignment of their magnetization directions. This effect is known as tunneling magnetoresistance (TMR). In order to explain this effect, Jullière proposed a model

based on the assumption that the transmission probability through the barrier is independent of spin and depends only on the electronic properties of the electrodes involved. For small bias voltages and in the absence of spin-flip scattering during the tunneling process, majority (minority) electrons in one electrode tunnel into majority (minority) states in the other electrode, in the case of a parallel alignment of the magnetizations of the electrodes. In the case of antiparallel alignment, electrons of majority character in one electrode tunnel into minority states of the second electrode. The two cases are shown schematically in Fig. 2.2. Thus the tunneling current flowing through the barrier is spin-polarized. Using the assumptions of Jullière, this tunneling current is proportional to the product of the DOS at the Fermi level of both electrodes. For the parallel alignment it can be expressed as

$$I_{\uparrow\uparrow} \propto \rho_{\uparrow}^s \rho_{\uparrow}^t + \rho_{\downarrow}^s \rho_{\downarrow}^t \quad (2.9)$$

while for the antiparallel alignment

$$I_{\uparrow\downarrow} \propto \rho_{\uparrow}^s \rho_{\downarrow}^t + \rho_{\downarrow}^s \rho_{\uparrow}^t \quad (2.10)$$

where $\rho_{\uparrow(\downarrow)}^{s(t)}$ are the spin-up (spin-down) DOS of the electrodes. This model, though much simplified by the assumptions therein, still describes the spin dependent tunneling process qualitatively.

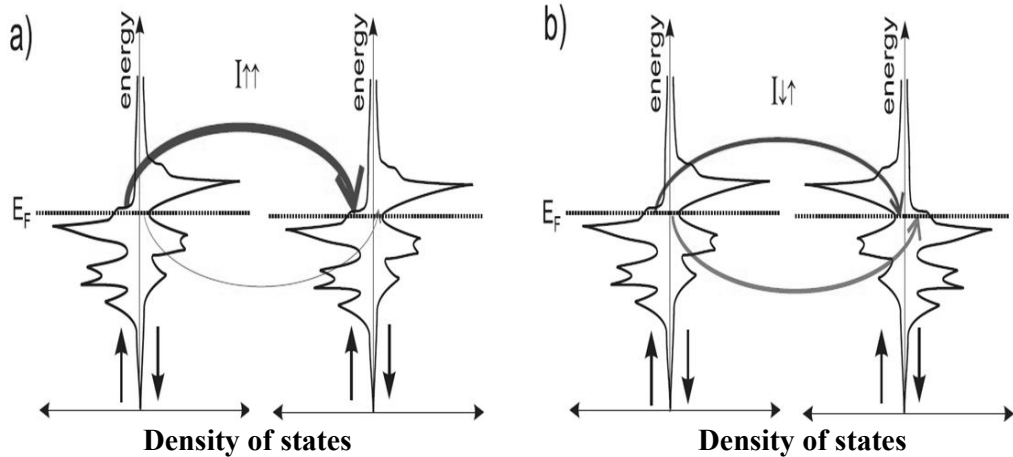


Fig. 2.2: Spin-polarized tunneling between two ferromagnetic electrodes for (a) parallel alignment of their magnetizations and (b) antiparallel alignment of their magnetization. The curved arrows indicate the tunneling current from left to right. Figure adapted from ref. [36]

A more elaborate description of the spin-dependent tunneling process was given by Slonczewski [37], who analyzed the spin-dependent tunneling current through a rectangular barrier by assuming a free electron model for the tunneling electrons. He showed that the tunneling current depends not only on the spin polarization of the two electrodes but on the nature of the barrier as well. He calculated the spin-dependent tunneling current in terms of the angle θ between the magnetization directions of the two electrodes and their respective spin polarizations:

$$I = I_o (1 + P_s P_t \cos \theta) \quad (2.11)$$

where I_o is the tunneling current without the spin polarization of the electrodes, P_s and P_t are the spin polarizations of the electrodes which are defined by

$$P_{s(t)} = \frac{\rho_{\uparrow}^{s(t)} - \rho_{\downarrow}^{s(t)}}{\rho_{\uparrow}^{s(t)} + \rho_{\downarrow}^{s(t)}} \quad (2.12)$$

The quantity $P_s P_t \cos \theta$ is the spin polarization of the tunneling current.

To get information about the spin polarization of a sample surface, the STM tip is usually coated with a magnetic material before scanning the surface. First attempts at spin-polarized STM (Sp-STM) using ferromagnetic tips were done by Johnson and Clarke [38] in 1990. They used Ni tips whose magnetization direction was fixed while the magnetization direction of their permalloy sample was periodically switched at a frequency higher than the cut-off frequency of the STM feedback loop. By detecting the modulation in the tunneling current through a lock-in amplifier they could prove the magnetic origin of tunneling current. The problem with their experiment is that it was performed in air without scanning and the significant magnetostriction on the Ni tips made it difficult for any imaging. Since the tunneling current contains both magnetic and nonmagnet information, the key task is to be able to separate them. The following discussion briefly presents the various modes of operation of a Sp-STM which had been suggested by Pierce [39] and have all been experimentally realized [10, 40, 41].

The Constant Current Mode

This is by far the simplest mode of operation but most difficult in terms of separation of nonmagnetic signal from the magnetic signal. The tip-to-sample distance is adjusted by the feedback loop in order to keep the tunneling current constant while the tip scans the sample surface producing a topographic map of the surface. If the tip is magnetic, this topographic map contains both spin-dependent and spin-independent components of the tunneling current. The magnetic effect, if significant, will appear as extra modulations in the topography. So by carefully comparing the topography obtained with nonmagnetic and magnetic tips these extra features in the topography can be deciphered. Wiesendanger *et al.* [10] obtained the first results using this mode. On the layered antiferromagnetic Cr(001) surface they found that the step height alternates between 0.16 nm and 0.12 nm when a ferromagnetic CrO₂ tip was used but obtained the expected step height of 0.14 nm when W tips were used. This was attributed to the TMR effect. Since Cr is a layered antiferromagnet, adjacent terraces have opposite spin polarizations. The tunneling current is enhanced on the terrace that has its spin polarization parallel to that of the tip and lowered on the adjacent terrace leading to the alternating step heights observed with the CrO₂ tip. This mode of operation turns out to be quite useful for atomic-scale Sp-STM studies of surface spin structures. It has been used to resolve the spin structures of antiferromagnetic metal nitrides [42], two dimensional antiferromagnetic metal layers [40, 43, 44], and ferromagnetic oxides [45].

The Spectroscopic Mode

The spectroscopic mode, otherwise known as spin-polarized scanning tunneling spectroscopy (Sp-STs), was realized in 1998 by Bode *et al.* [40] and allows to a certain extent the separation of topographic information from spin information. In this mode, the spin-resolved differential conductance dI/dV which is proportional to the spin polarized LDOS is measured with a magnetic tip (usually a W tip coated with ferromagnetic or antiferromagnetic thin film such as to minimize the stray field from the tip). The differential conductance is measured by adding a small a.c. modulation to the d.c. bias at a frequency slightly higher than the cut-off frequency

of the STM feedback and detecting the resulting modulation of the tunneling current due to the change in bias voltage through a lock-in amplifier. By choosing the bias voltage between the magnetic tip and magnetic sample in such a way as to maximize the tunneling into or out of highly spin-polarized states, a high spin contrast image can be obtained. This method is widely used by many groups doing Sp-STM. Atomic resolution has been achieved in some cases as in the two dimensional antiferromagnetic Fe monolayer on W(001) [44] and very recently to measure the magnetization curves of individual Co atoms on Pt(111) [46]. The main disadvantage of this mode is the weak dependence of the dI/dV signal in Sp-STS on the local magnetization DOS. The differential conductance in Sp-STS can be expressed as [47]

$$\frac{dI}{dV} \propto \rho_t \rho_s(\vec{R}_t, E_F + eV) + \vec{m}_t \vec{m}_s(\vec{R}_t, E_F + eV) \quad (2.13)$$

where $\rho_{t(s)}$ is the LDOS of the tip (sample) and $m_{t(s)}$ the magnetization of tip (sample) at the location of the tip R_t . Thus V , the applied voltage must be chosen so as to maximize m_s over ρ_s . The strong dependence of the dI/dV signal in this mode on ρ_s limits its use to surfaces with a homogeneous electronic structure [48].

The Differential Magnetic Mode

In the spirit of Johnson and Clarke [38], Wulfhchel and Kirschner [49] performed the first successful experiments using this mode in UHV in 1999. When the magnetization direction of the tip is periodically switched at high frequency, the tunneling current is also modulated at the same frequency due to the TMR effect. Thus a differential magnetic conductivity dI/dM can be obtained which is proportional to the component of the sample spin polarization in the direction of the tip spin polarization [47]. In the experimental setup (described in the next chapter), a bulk ferromagnetic tip whose magnetization can be switched periodically between two stable configurations by an alternating current through a coil fixed to it is used. Depending on the shape of the tip, it is possible to obtain out-of-plane (when the tip is in the form of a needle) or a well defined in-plane (when the tip is in the form of a ring) magnetic sensitivity. The key point here is

that the frequency of switching of the magnetization of the tip is much higher than the cut-off frequency of the STM feedback loop. In this way the feedback loop only detects the average tunneling current which is independent of any spin information while the modulation in the tunneling current introduced by the tip switching is detected through a phase sensitive lock-in amplifier and contains all the spin information. Thus topography and spin data are acquired simultaneously and clearly separated. This is the main advantage of this mode, as well as the fact that the magnetization direction of the tip can be well defined (as in the case of the ring electrode). The disadvantage here is that no magnetic field can be applied to the sample during a measurement, as this will affect the magnetic switching of the tip. The Sp-STM experiments in this thesis will be restricted to this mode.

Chapter 3

Experimental Setup

Experiments designed to investigate the physical and chemical properties of a surface whose composition is representative of the bulk, require the preparation of a clean surface and maintaining such a surface within the time limit to perform the experiments. This requires ultrahigh vacuum (UHV) conditions, that is, pressures in the 10^{-9} mbar range and below. This is because surface properties are very sensitive to contamination and only such low pressures ensure that the surface stays clean long enough to perform an experiment. For example, the rate of molecules

impinging on a surface is given by $R = \frac{P}{\sqrt{2\pi mkT}}$ $\text{cm}^{-2}\text{s}^{-1}$, where m is the molecular

mass, k is Boltzmann constant and T the temperature. Typical values of R for the residual gases (CO , H_2 , O_2 , CO_2 , H_2O) commonly found in UHV chambers are between 10^{14} to 10^{15} $\text{cm}^{-2} \text{s}^{-1}$. Thus for a pressure of 10^{-6} mbar at 300K a surface (which usually contains about 10^{15} atoms per cm^2) can only stay clean for one second or so. For the experiments reported here, it is essential to maintain the pressure of the system within the 10^{-10} mbar range. This section describes the UHV chamber and the various surface analysis tools used therein, most of which only operate under UHV conditions.

3.1 The ultrahigh vacuum chamber

The experiments were carried out in an UHV chamber equipped with an Auger electron spectrometer (AES), a low energy electron diffractometer (LEED) and a spin-polarized scanning tunneling microscope (SP-STM) custom-made from an OMICRON room temperature scanning tunneling microscope (see Fig. 3.1).

The entire system consists of the main chamber and a two stage load-lock chamber that can each be pumped separately. In this way samples (and STM scanners) can be effectively exchanged within a 3-4 hour period without breaking the vacuum. In the main chamber, the sample preparation section is linked to the STM section by a wagon that can be moved on a rail to transfer samples to and from the preparation section. The pressure in the main chamber (less than 1×10^{-10} mbar) is achieved through a two-stage pumping system consisting of a turbomolecular pump and an ion getter pump (backed by a Ti sublimation pump). In the preparation section, the AES gun is located opposite the LEED screen.

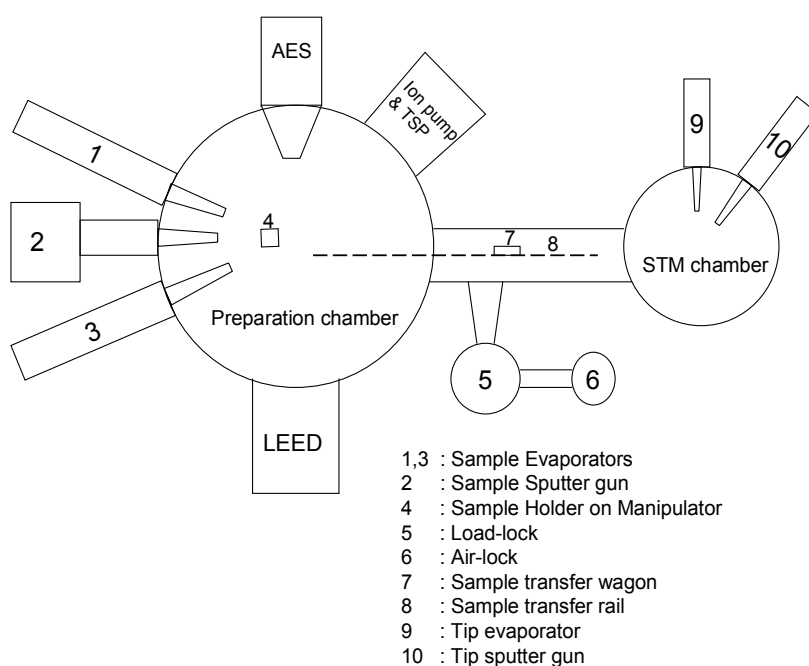


Fig. 3.1: Lay-out of the multipurpose chamber used in the experiments. The oxygen leak valve was installed in the load-lock chamber to allow oxygen exposure of the sample while preventing oxygen contamination of the tip.

In this way, the combination of the AES gun and the LEED optics can be used as a medium energy electron diffractometer (MEED) to monitor film growth during deposition. A brief description of the various surface analysis techniques used in the system is given below.

Auger Electron Spectroscopy (AES)

This technique is based on the Auger process named after the French scientist Pierre Auger who first observed it in the 1920s [50]. In an AES experiment, the sample is bombarded with high energy electrons of some KeV creating holes in the core levels of the atoms of the sample. These holes are filled by electrons from the outer shells of the atom and the energy released is transferred to another outer electron which is then ejected from the atom (the so-called Auger electron). Since the energy of the Auger electron depends only on the energy levels of the atom involved and not on the energy of the impinging electrons it is thus an element specific process. It is also surface sensitive as the energy of the Auger electrons is low. Thus the escape depth of the electrons is only limited to within a few monolayers of the surface under investigation. AES is widely used to check the cleanliness of surfaces and to determine the chemical composition of adsorbates.

Low Energy Electron Diffraction (LEED)

LEED is particularly used to determine surface structures either qualitatively, where the positions of the diffraction spots give the size and symmetry of the surface unit cell (and also that of an adsorbate with respect to the substrate in the case of a thin film), or quantitatively, where the analysis of the spot intensities as a function of the incident electron energy provides information on the exact position of the atoms. Diffraction is observed in this case because the low energy of the electrons used in the experiment (typically 30 to about 500 eV) gives the electrons de Broglie a wavelength comparable to interatomic distances [51]. Electrons with energy 200 eV have a de Broglie wavelength of 0.87\AA . In matter, the mean free path of these low energy electrons is small ($\sim 5 - 10\text{\AA}$), such that LEED is surface sensitive and only near surface electrons can backscatter in the sample.

Medium Energy Electron diffraction (MEED)

In our set-up the auger gun is placed opposite the LEED screen such that one can perform diffraction experiments with the energy of 5 keV in grazing angle geometry using the Auger gun as the source of the primary beam. The grazing angle reduces the penetration depth of the electrons and ensures surface sensitivity.

By monitoring the variation of the intensity of the specular spot with deposition time one can effectively determine the film thickness. During layer-by-layer growth, the intensity shows an oscillatory behavior related to the periodic change in the film roughness [18].

3.2 The spin-polarized STM setup

The spin-polarized STM used in the experiments is a modified version of an OMICRON Micro STM [52]. The STM uses piezoelectric materials to control the movement of the tip in a very precise and accurate way. These materials have the property that their length can be slightly altered in the presence of an electric field. The piezoelectric coefficients of the piezos used are in the range of 10nm/V (a voltage of say 1 mV will cause a change of distance of 0.1 Å). By applying a constant voltage to the piezo, the tip can be brought to a few angstroms from the sample surface. The STM used in the experiments reported here uses a tube scanner. In this geometry, the inside and outside of the tube are coated with thin metal electrodes. The outside is separated into four sections (X+, X-, Y+, Y-) which are electrically isolated from each other. A motion in the z-direction (along the tube longitudinal axis) is achieved by applying a voltage between the inside and outside of the tube while lateral motion is achieved by applying the voltage across the tube. In most cases the STM tip is kept at a constant distance from the sample surface as the surface is scanned. To make sure this distance is always constant a feedback mechanism is used to regulate the voltage supplied to the piezo. When the tip is held at a small distance to the sample surface, a tunneling current flows between the tip and sample. The feedback electronics measures the deviation of the tunneling current from the set value and adjusts the tip accordingly. If the tunneling current becomes larger, it retracts the tip or advances the tip, when the current becomes smaller. By recording the z piezo voltage $V_z(x,y)$ at every pixel (x,y) , the morphology $z(x,y)$ of the surface can be mapped.

$$z(x,y) = c_z V_z(x,y) \quad (3.1)$$

where c_z is the piezo coefficient. Under favorable conditions the STM can detect single atoms, hence it is the tool with the ultimate lateral resolution for imaging magnetic nanostructures if the tip is magnetic.

Magnetic sensitivity is achieved in our set-up by using a modulation technique which is shown schematically in Fig. 3.2. The STM electrode, which is in the form of a ring, is sensitive to the in-plane component of the sample spin polarization due to shape anisotropy (i.e. the magnetization direction of the ring is tangential to its outer perimeter due to its shape). With a coil wound around the ring, the ring magnetization direction can be periodically switched between two stable configurations by a sinusoidal current applied through a phase sensitive lock-in amplifier. The frequency of this current (between 20kHz and 40 kHz) is chosen to be much larger than the cut-off frequency of the STM feedback loop, hence the feedback loop cannot detect changes in the tunneling current due to this switching of the tip magnetization. The feedback loop only detects the average tunneling current which gives the topography while high frequency changes in the tunneling current are detected in the lock-in amplifier and give the spin polarization of the sample surface in the direction of the tip magnetization. In this way the sample topography and spin polarization can be separated and measured simultaneously.

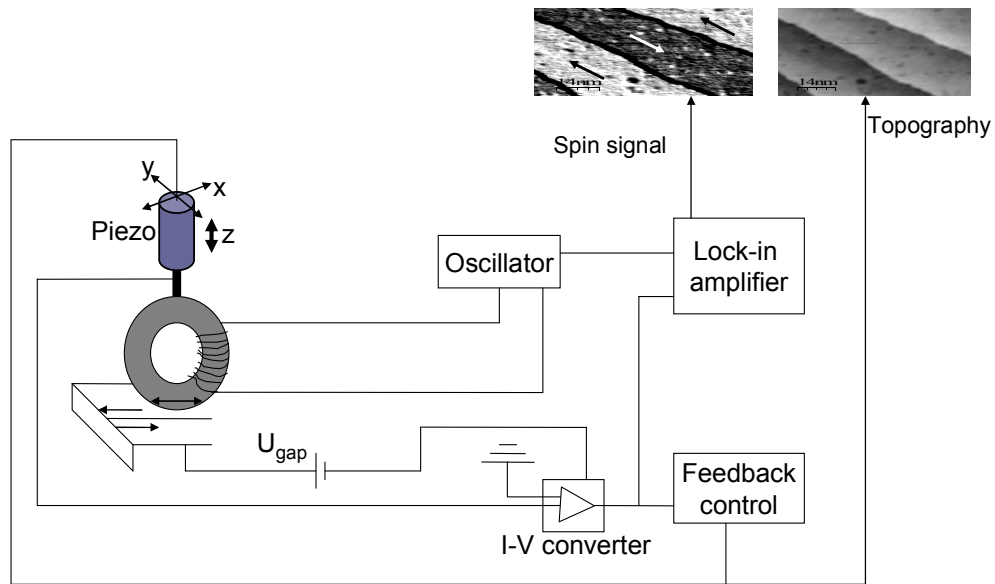


Fig. 3.2 : Circuit diagram of the spin polarized STM showing how the topography and spin signal are separated.

The tunneling current in the case of a magnetic tip and a magnetic sample depends on the spin polarization of the tip P_T and sample P_S and on the relative orientation of their magnetization. This can be written as [37]

$$I_{\uparrow\uparrow} = I_0 (1 + P_T P_S \cos\theta) \quad (3.2)$$

where θ is the angle between the magnetization directions of the tip and sample. When the tip magnetization direction is reversed equation (3.2) becomes

$$I_{\uparrow\downarrow} = I_0 (1 - P_T P_S \cos\theta) \quad (3.3)$$

The average of these two cases

$$(I_{\uparrow\downarrow} + I_{\uparrow\uparrow})/2 = I_0 \quad (3.4)$$

is purely a direct current independent of spin. This is the component that is extracted from the STM feedback loop and gives the topographic information.

The difference

$$\Delta I = (I_{\uparrow\uparrow} - I_{\uparrow\downarrow}) = 2I_0 P_T P_S \cos\theta \quad (3.5)$$

contains the spin information and it is detected in the lock-in amplifier. In a real experiment the average tunneling current I_0 is kept constant. In this case $\Delta I/2I_0$, the spin signal, is proportional to the projection of the sample spin polarization onto the direction of magnetization of the ring. The spin contrast is the difference in the spin signal measured between two oppositely magnetized neighboring domains.

Preparation of ring-shaped STM tips

The choice of material for the tip is crucial. The material should have a low coercivity so that only a small magnetic field is necessary to switch its magnetization without affecting the magnetization of the sample surface and also prevent local heating of the tip. It should also have a vanishing magnetostriction such that no changes in the length and shape of the tip occur during the magnetization reversal. These properties are met in the Co-rich amorphous alloy FeCoBSi which is commercially available. The rings are electrochemically etched from a FeCoBSi foil of 25 μm thickness. A detailed description of the etching process can be found in ref. [53]. After etching and polishing the ring has an outer diameter of about 2mm. A coil of about 20 turns (made from an insulated copper wire of 50 μm thickness) is manually wound on the ring to switch its magnetization

when an alternating current is applied to the coil. The coil is electrically connected to the STM scanner through two gold contacts attached to the scanner. The ring is fixed to the scanner via a Ta wire glued to the ring with silver paste. After transfer to the chamber the ring is cleaned by Ar^+ sputtering for a few hours. This process is repeated for a few minutes before every experiment. During scanning the tip can be improved by applying voltage pulses to it. To increase the size of the spin signal some iron is usually deposited on the outer perimeter of the ring used for tunneling before each spin polarized measurement.

To make sure the ring works properly we test it on the Mn/Fe(001) system which has been studied by many groups as well in our lab [54-56]. It is known that Mn is a layered antiferromagnet when stabilized epitaxially on bcc Fe(001), so one would expect an alternating contrast in the spin signal from one Mn layer to the next. Fig. 3.3 shows the topography and corresponding spin image for a 7 monolayer (ML) Mn film grown on Fe(001) clearly displaying the contrast between adjacent Mn layers. A freshly prepared ring can work properly for a few months after which it becomes unstable as some of the insulation on the copper coil is removed due to repeated sputtering.

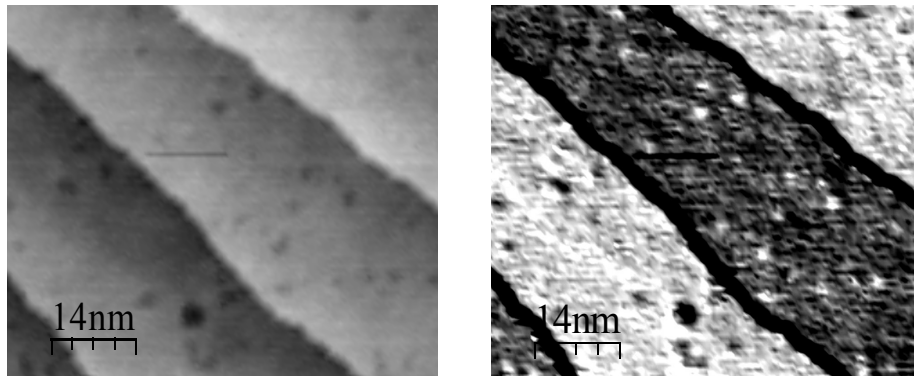


Fig 3.3: 7ML Mn on Fe(001) used as a test for the ring. The image on the left represents the topography while that on the right is the spin signal. Four layers are exposed which show alternating contrast in the spin signal.

3.3 In-situ sample preparation

Iron whiskers were used as the substrate in the experiments. Compared to iron crystals grown from the melt these, whiskers are grown from the vapor phase and contain fewer impurities, have larger terraces of several hundred nanometers and a simple magnetic domain structure. The whiskers used in the following experiments have a rectangular cross section, are quite thin (a few hundred microns thick) and only a few centimeters in length. In order to effectively mount the whiskers on a Molybdenum sample plate without deforming it, a small groove ($10 \times 0.5 \times 0.3$) mm was laser-drilled in the plate and the whisker was placed inside. It was then covered and fixed at one end with a 0.2 mm Mo foil. After transfer into the UHV chamber, the whiskers were cleaned by several cycles of Ar^+ sputtering at 2.0 keV and annealing to about 700K. Sputtering while ramping the temperature slowly up to 700K was found to effectively remove contaminants like sulfur, carbon and oxygen which segregate to the surface from the bulk at different temperatures. The sputtering was done until no contaminants could be detected by AES and LEED exhibited a sharp (1×1) pattern as shown in Fig. 3.4.

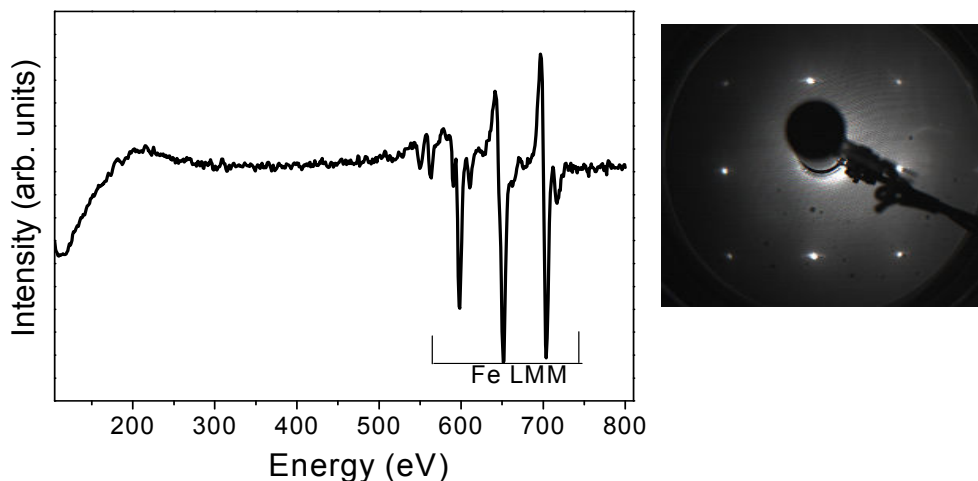


Fig. 3.4: Left: Auger spectrum of clean Fe whisker. Right: LEED pattern of clean Fe whisker taken at 70 eV.

The films on both the substrate and tip were deposited by electron beam evaporation. In this process, the growth material is heated to evaporation condition by electrons accelerated from a heated filament. For deposition of Fe on the ring, a 2 mm thick Fe rod was used while for Mn on the Fe whisker a crucible containing Mn flakes was used. This was necessary as Mn rods were found to degas considerably during deposition (the pressure sometimes went up to 5×10^{-9} mbar during evaporation of Mn rods). The evaporators are water-cooled during film growth to minimize gas desorption from them.

Chapter 4

Oxygen on Fe(001)

The adsorption of foreign atoms on the surface of a magnetic material may lead to the rearrangement of the atoms at the surface and a change in the separation between atomic planes. This has far reaching consequences on both the adsorbed atoms as well as the host material. In particular, if the adsorbed atom is nonmagnetic, one may also observe in addition to the structural changes a modification of the magnetic structure of the surface atoms of the host material. In some cases an enhancement of the Curie temperature has been reported [28] as well as an inducement of a magnetic moment on the otherwise nonmagnetic adsorbate [57]. A case of interest is the adsorption of oxygen in an ordered monolayer on the surface of bcc Fe(001). This system has been extensively studied experimentally with photoemission and inverse photoemission [25, 58-61] for many years as well as with *ab initio* theoretical calculations [15, 62-65]. Due to the enhanced spin-dependent exchange scattering from the oxygen covered iron surface, it has been proposed and used in spin detectors [66]. The advantage of scanning tunneling microscopy in probing adsorbate states on surfaces is the fact that it is a local technique and can probe the LDOS in the vicinity of individual adsorbates and defects [67]. In this Chapter the focus will be on Fe(001)-p(1x1)O, an ordered monolayer of oxygen adsorbed on bcc Fe(001) investigated by spin-polarized scanning tunneling microscopy and spectroscopy.

4.1 Preparation of Fe(001)-p(1x1)O

The initial stage for the preparation of this surface involves first obtaining a clean Fe(001) surface which has been described briefly in Chapter 2. Initially, the whisker is sputtered for several hours with 2.0 keV Ar⁺ at room temperature. This is followed by several sputter-anneal cycles (up to 700K). Since the native impurities in the whisker (mainly sulfur, phosphorus, carbon and oxygen) segregate to the surface at different temperatures, these impurities were removed by sputtering while slowly increasing the temperature up to 700K. After a few days of

this process, STM images of the whisker (Fig. 4.1) showed smooth surfaces with terraces several hundreds of nanometers wide and AES showed no traces of any impurities within the detection limit (see Fig. 3.4).

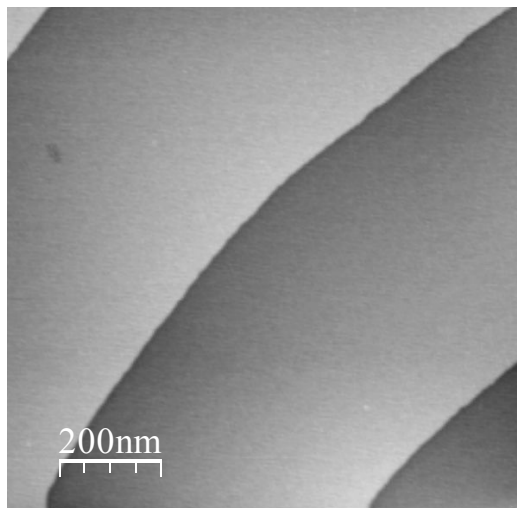


Fig. 4.1: STM image of clean Fe(001) whisker surface taken at $I=3.0$ nA, $V=0.5$ V

It is generally agreed that oxidation of iron occurs in three stages: dissociative chemisorption of O_2 , incorporation of O atoms in the selvedge and formation of three-dimensional bulk oxides. However, experimental studies on the adsorption of oxygen on Fe(001) sometimes give varying opinions especially regarding the thermodynamically stable surface structure and saturation coverage at the completion of the chemisorption stage. While some groups report a (1×1) structure up to a monolayer of oxygen [68-70] others report a $c(2\times 2)O$ structure at the chemisorption stage [60, 71]. However, as pointed out by Legg *et al.* [68] and Leygraf and Ekelund [69], the $c(2\times 2)$ structure is weak and is observed only in the presence of C impurities, thus can be attributed to C rather than oxygen alone.

In the experiments reported here, the adsorption was done at room temperature and the sample was annealed to 700K. The procedure was as follows: the Fe(001) whisker was cleaned and checked by LEED and AES, Oxygen exposure was carried out at 5.0×10^{-8} mbar by letting in 99.999% pure O_2 gas into the chamber at room temperature using a leak valve. The surface was then heated to 700K (to

remove excess oxygen) and checked with LEED, AES and STM. This procedure was repeated for different oxygen exposures in order to obtain the oxygen exposure necessary to complete the chemisorption stage. The exposure is given in units of Langmuir (L), where $1\text{L} = 1.33 \times 10^{-6} \text{ mbar s}$. In general, the surface was cleaned before each oxygen exposure and the exposure was done in the load-lock chamber to prevent contamination of the STM tip in the main chamber.

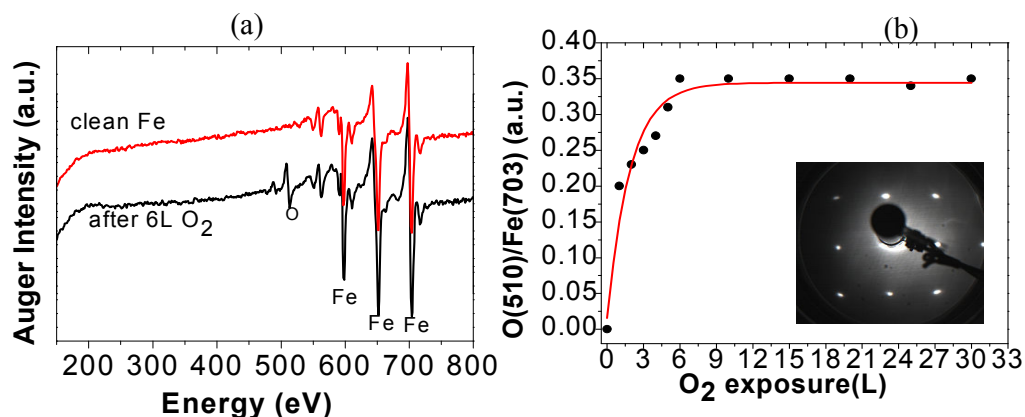


Fig. 4.2: (a) Auger spectra for clean Fe(001) surface and after exposure of 6L oxygen, (b) Ratio of the O 510 eV Auger peak to the Fe 703 eV peak as a function of oxygen exposure (the red curve is a guide to the eye). The inset shows the LEED pattern after exposure to 6L oxygen.

Figure 4.2(a) shows the Auger spectra for clean Fe(001) and the same surface after exposure to 6L oxygen. The principal oxygen Auger peak can clearly be seen at 510 eV, which is absent in the case of the clean Fe(001) surface. By monitoring the ratio of the oxygen 510 eV Auger peak to the iron 703 eV Auger peak as a function of oxygen exposure, it is observed that the ratio increases rapidly with oxygen exposure up to about 6L where it reaches a saturation value of approximately 0.35. Similar values were reported for segregated oxygen [58, 72] and for 6L oxygen on Fe(001) [70]. The LEED pattern was always (1×1), but for oxygen exposures above 6L the background increased significantly with a subsequent disappearance of the LEED pattern above 20L oxygen.

Constant current STM images of the surface (shown in Fig. 4.3) after different oxygen exposures reveal that already at 6L the surface topography

changes, as evident by the kinks that appear along the step edges (see Fig 4.3(a)). This is a precursor to oxidation due to incorporation of some oxygen atoms into the subsurface region. After 10L small oxide patches can be seen along the step edges as well as on the terraces (Fig. 4.3(b)). At 25L oxygen three-dimensional oxide islands could be identified on the surface (Fig 4.3(c)).

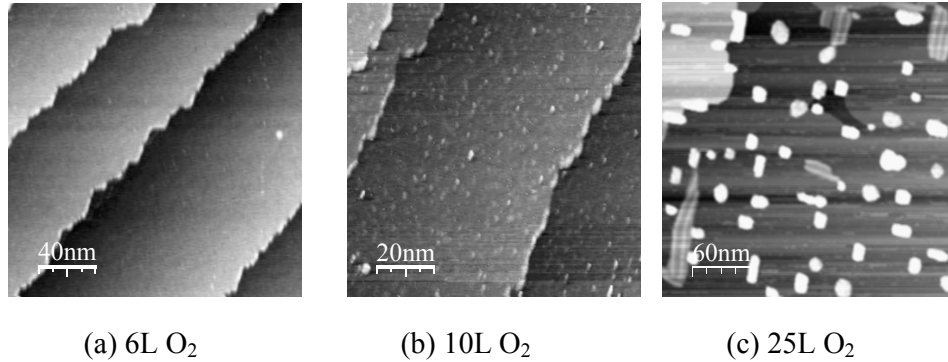


Fig. 4.3: Constant current STM images of Fe(001) surface exposed to 6L, 10L and 25L oxygen, respectively. All images were taken at $I_t=3.0$ nA and $V = 0.1$ V

Thus 6L oxygen has been used as the exposure necessary to complete the chemisorption stage above which oxidation of the Fe(001) surface begins. At this stage the adsorbed oxygen atoms form a (1×1) layer and occupy the four-fold hollow sites on the Fe(001) surface [68, 73, 74].

4.2 The Fe(001)-p(1×1)O surface: Structure and Magnetism

The structure of the Fe(001)-p(1×1)O surface is known from LEED studies by Legg *et al.* [68, 74] and Chubb and Pickett [73]. The structural model proposed by Legg *et al.* is presented in Fig. 4.4. It shows the oxygen adsorption site as well as the interlayer distances. The O atom slips deep into the hollow site such that the first Fe layer Fe(S) is raised with respect to the second Fe layer Fe(S-1). In this subsection, a real space representation of the surface structure is presented from atomically resolved spin-polarized STM data.

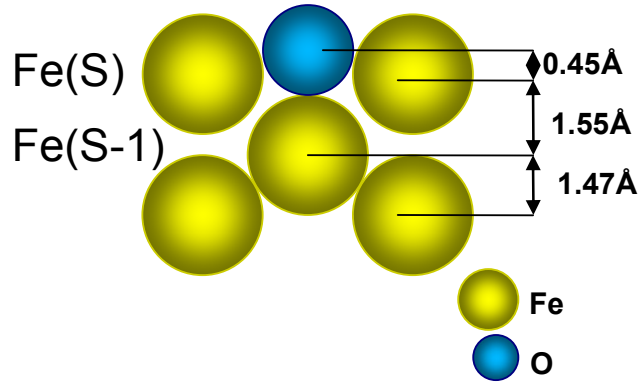


Fig. 4.4: Structural model for Fe(001)-p(1×1)O from LEED [74]. The O atoms occupy the four-fold hollow sites about 0.45Å above the surface. Fe(S) and Fe(S-1) represent the surface and subsurface Fe, respectively.

All the STM images presented in this thesis were taken at room temperature using ferromagnetic ring electrodes as the probe tip. Figure 4.5(a) presents an atomically resolved constant current STM image of the Fe(001)-p(1×1)O surface showing a slightly distorted square array of protrusions including some point defects. The protrusions are identified as oxygen atoms at the four-fold hollow sites, as discussed later. The slight deviation from a square lattice is due to thermal drift of the scanner during scanning. The line scan in Fig. 4.5(b) is taken along the line in (a) and shows a corrugation of about 0.2 Å.

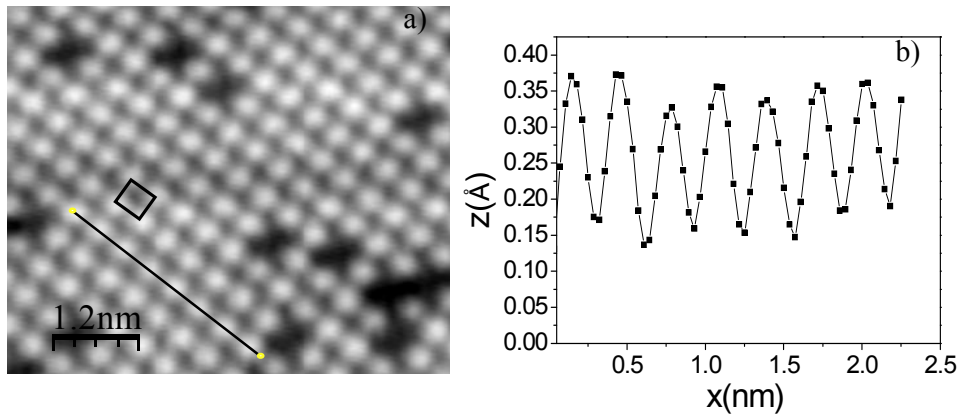


Fig. 4.5: (a) Atomically resolved STM image of the Fe(001)-P(1×1) surface, $I_t=3\text{nA}$, $V=0.3\text{V}$. The square marks the surface unit cell. (b) Line scan along the line shown in (a)

There was no contrast reversal in the atomically resolved constant current STM images in the whole range of voltages (-1V to +1V) used in the experiment except for a change in the corrugation amplitude as shown in Fig. 4.6. The corrugation amplitude decreases rapidly with increasing voltage. This is because at smaller voltages, in order to maintain a constant tunneling current, the tip-to-sample distance is reduced by the feedback mechanism, giving rise to a larger corrugation as the tip gets closer to the surface. The non reversal of the topographic contrast implies that the STM is consistently imaging the O atoms as the bright protrusions.

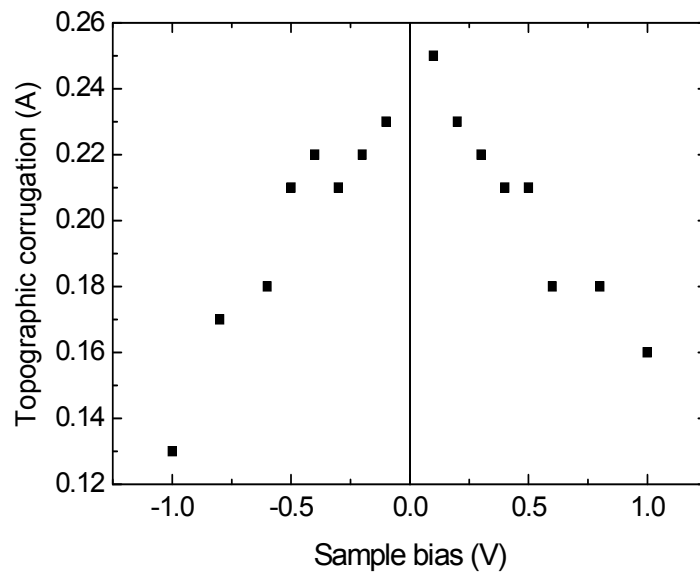


Fig. 4.6: Variation of topographic corrugation with applied voltage. All the atomically resolved images used were acquired at $I = 3$ nA.

The atomically resolved STM data can be compared with the LEED model. Unfortunately it was not possible to image the subsurface iron atoms so we can only restrict ourselves to the surface plane. The average distance between the protrusions in Fig. 4.5(a) is 0.293 ± 0.005 nm, comparable to the lattice constant of bcc Fe of 0.287 nm. The Fourier transform of the STM image is consistent with the LEED pattern (see Fig. 4.7). Hence the location of the protrusions in the STM images represents the four-fold hollow sites of the surface.

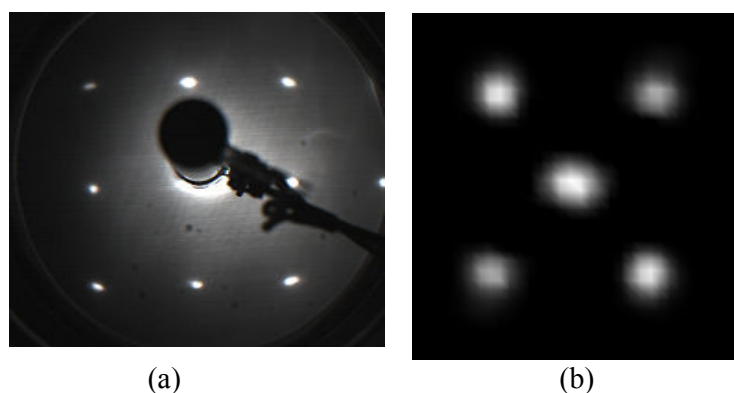


Fig. 4.7: (a) LEED pattern of Fe(001)-p(1×1)O (b) Fourier transform of the atomically resolved STM image of Fig. 4.5(a)

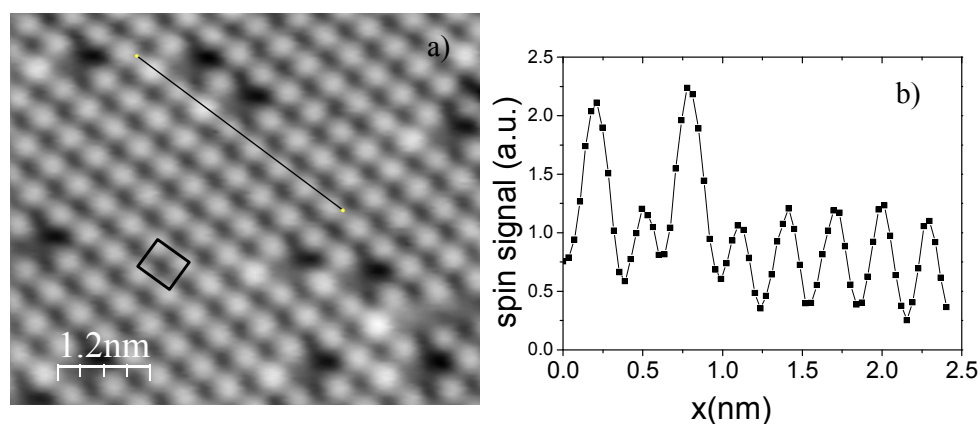


Fig. 4.8: (a) Spin image acquired simultaneously with the topography in Fig. 4.5. (b) Line scan along the line in (a)

The spin image obtained simultaneously with the topography in Fig. 4.5(a) is given in Fig. 4.8(a). It has the same periodicity as the topography and the maximum spin signal is above the oxygen adsorption sites. Close to point defects (which in this case are missing O atoms) the spin signal is enhanced as seen in the line scan (Fig. 4.8(b)) and also in the spin image (Fig. 4.8(a)), where the atom adjacent to the defect appears brighter. The same effect is observed irrespective of the scan direction (forward or backward scan) and for different tips. On the ideal oxygen-terminated surface, the O atomic orbitals are conductive due to hybridization of O

p -states with Fe d -states thereby causing the surface O atoms to become spin-polarized. In the presence of defects (missing O atoms in this case), this spin polarization is altered locally due to changes in the p - d orbital hybridization. This may result in the enhancement of the spin polarization at atomic sites adjacent to the defects.

4.3 Sp-STs on Fe(001)-p(1×1)O

Scanning tunneling spectroscopy measurements were performed to check the electronic structure of the Fe(001)-p(1×1)O surface. The measurements were first performed on the clean Fe(001) surface in order to see any changes induced by the oxygen adlayer. All measurements were done at room temperature by applying an a.c. modulation (of amplitude 30 mV at a frequency of 6.5 kHz) to the d.c. bias voltage and detecting changes in the differential conductivity dI/dV directly through a phase sensitive lock-in amplifier. As mentioned in Chapter 2, the differential conductivity is proportional to the local density of states (LDOS) of the sample at the position of the tip for states close to the Fermi level. Thus features in the dI/dV spectra can be compared to those in the computed DOS of the sample surface. The differential conductivity spectrum for a clean Fe(001) surface is shown in Fig. 4.9. The dI/dV signal has been normalized with I/V to reduce the exponential background due to the tip-sample separation dependence on the tunnel current. A peak is seen at 0.15V in agreement with Bischoff *et al.* [75] and Stroscio *et al.*[76]. This peak corresponds to a minority spin surface state on Fe(001) which originate from unperturbed d -orbitals extending into the vacuum.

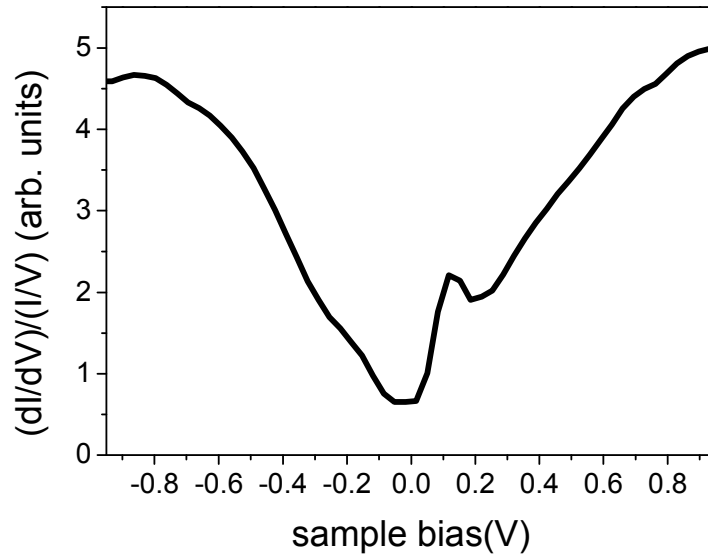


Fig. 4.9: dI/dV spectrum normalized with I/V for clean Fe(001). The spectrum was acquired at a setpoint $V = -0.9$ V, $I = 3$ nA.

In comparison to the clean Fe(001) surface, the differential conductance spectrum of Fe(001)-p(1×1)O (Fig. 4.10) shows a new broad peak around -0.7V, and a smaller peak very close to the Fermi energy. The peak observed at 0.15V on the clean surface is now shifted to slightly higher energy and is almost quenched. It only shows up as a shoulder around 0.27V. A similar result was obtained by Bischoff *et al.* [75], who found a slight shift to higher energy for the minority spin surface state and a 30% reduction in the peak amplitude at isolated oxygen impurities on Fe(001). The peak at -0.7V has not been reported before in spectroscopy experiments for this surface.

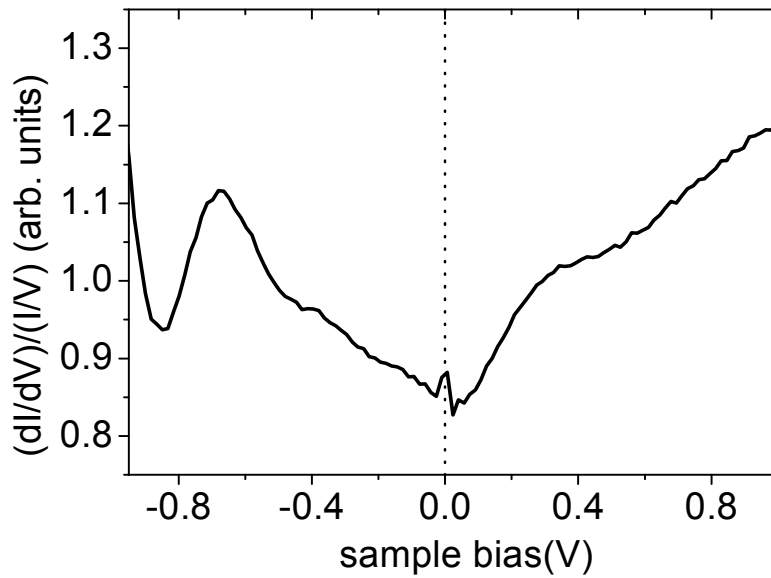


Fig. 4.10: Differential conductivity spectrum for Fe(001)-p(1×1)O obtained at the setpoint $V = -1$ V, $I = 3$ nA

4.4 Discussion

4.4.1 Identifying the atomic registry of Fe(001)-p(1×1)O from STM

It is generally not straight forward to chemically identify individual adsorbates in atomically resolved STM images because it is unclear just by looking at the images whether the contrast is dominated by geometric or electronic-structure effects. In other words, the fact that an adsorbed atom lies geometrically above the surface does not generally mean it appears as a protrusion in an STM topographic image. In order to identify whether the protrusions in the images represent the location of Fe or O atoms, the STM images have been compared to calculations on the same system performed by Wu and Freeman [77]. According to the Tersoff-Hamann approximation of the STM [33, 34], the tunneling current is proportional to the sample LDOS at the position of the probe tip. Thus plots of the charge density within the surface-vacuum region would be representative of the actual STM image. Plots of the charge density in the surface-vacuum region for a

(1×1) oxygen monolayer (ML) on 2ML Fe grown on W(001) is shown in Fig. 4.11, taken from ref. [77]. Fe(S) and Fe(S-1) represent surface and subsurface Fe, respectively, while O is surface oxygen. In the plots, the charge density contours extend higher above the four-fold coordinated oxygen atoms, thus confirming that the STM is imaging the oxygen atoms as protrusions on the Fe(001)-p(1×)O surface. The STM image is thus, a combination of geometric as well as electronic structure effects. The point defects in the STM image in Fig. 4.5 (a) therefore represent missing O atoms. Considering the number of missing O atoms in Fig. 4.5(a) one can estimate an oxygen coverage of about 95% which is consistent with the expected oxygen coverage of a full monolayer.

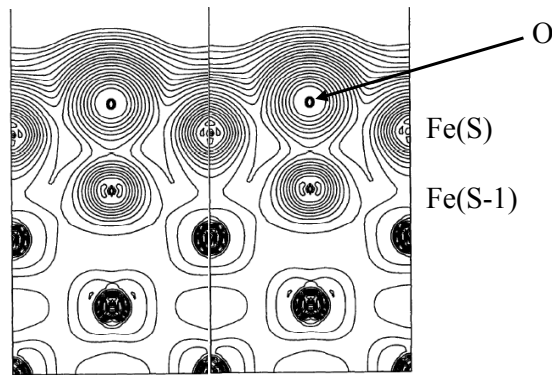


Fig. 4.11: Charge density plots for O/Fe showing strong corrugation in the surface vacuum region. The maximum charge density lies above the oxygen adsorption sites. The figure is taken from ref. [77].

4.4.2 Spin density from the Fe(001)-p(1×1)O surface

Figure 4.12 shows spin density contours for the system O/2ML Fe/ W(001) [77] which reveal positive spin density emanating from the oxygen sites (O) into the vacuum. This is consistent with the spin image of Fig. 4.8(a) which shows that the maximum spin signal is above the oxygen. The presence of oxygen on the surface causes a modification of the electronic structure of Fe(001). The exchange splitting of the Fe *d* bands and the hybridization between the oxygen *p* orbitals and Fe *d* orbitals induces a splitting of the oxygen states that bond with Fe. These states are partially occupied for majority spins and almost unoccupied for minority spins [78]. This results in a positive spin polarization in the DOS at the Fermi level and an induced magnetic moment at the oxygen sites.

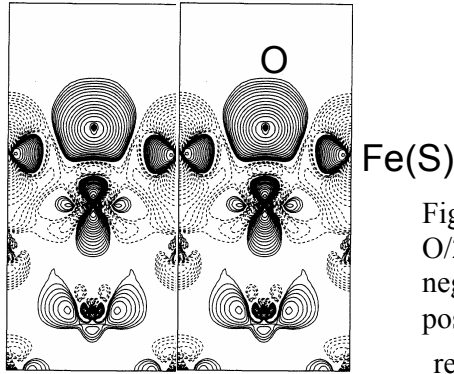


Fig. 4.12 Spin-density contours for the system O/2ML Fe/W(001), dashed lines represent negative spin density while full lines represent positive spin density. The figure is taken from ref. [77]

As shown in Fig. 4.8(a&b), there is an enhancement of the spin signal close to missing oxygen atoms. The situation is shown schematically in Fig. 4.13. However, the enhancement is observed only for the oxygen atom indicated as the brighter atom in Fig. 4.13. Since the surface is four-fold symmetric one would have expected the atoms at equivalent sites adjacent to the defect to have their spin polarization enhanced as well. This nonsymmetrical enhancement of the spin polarization close to the defects might be because of symmetry breaking.

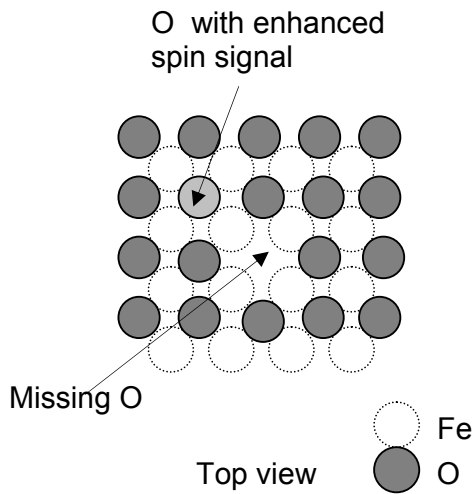


Fig. 4.13: Schematic of spin signal around a missing O atom. The position of the missing O atom and the atom with an enhanced spin signal are indicated with the arrows.

In the experiment, the direction of magnetization of the tip was fixed in the [100] direction which is parallel to the magnetization direction along the long axis of the Fe whisker. Firstly, the symmetry is broken by the magnetization of the whisker,

which was always parallel to the [100] direction in the scanned area. Possibly via the spin orbit interaction, the oxygen atoms experience a different spin polarization as a function of their position with respect to the defect. Secondly, when the tip scans over a vacancy, due to the size of the defect there is a contribution to the spin-polarized tunneling current not only from the last apex atom of the tip but from adjacent tip atoms as well. Thus there might be non-perpendicular tunneling near such defects resulting in the only one of the adjacent atoms having an enhanced spin signal.

4.4.3 Spin-resolved density of states of Fe(001)-p(1×1)O

In order to clarify the origin of the features observed in the differential conductance spectrum, calculations of the electronic properties of the Fe(001)-p(1×1)O system were performed using the scalar-relativistic Korringa-Kohn-Rostoker (KKR) Green function method [79, 80] with the local density approximation to density functional theory. The calculations were performed for a six layer Fe slab with an oxygen layer above the surface. The Vienna *Ab initio* Simulation Package (VASP) [81] was used for atomic relaxations and the results agree well with previous calculations and LEED measurements [68]. The calculations were done with the help of Dr. Arthur Ernst of the Max Planck Institute of Microstructure Physics in Halle, Germany.

The DOS in the vacuum region and for the surface layer in the energy range used in the experiment is shown in Fig.4.14. The top curve in Fig.4.14 shows the DOS in the vacuum region (within the Tersoff-Hamann model), about 4Å above the surface of Fe(001)-p(1×1)O. This distance is close to the tip-sample separation in typical experimental settings. The black and red curves represent the DOS for spin up and spin down electrons, respectively. It is clear from the plots that the majority spin channel dominates the DOS in the vacuum region. This also confirms the fact that the adsorption of oxygen induces a positive spin polarization on the Fe surface. The main feature in the DOS is a peak at -0.6 eV and a smaller peak at 0.05 eV. In the experiment (see Fig.4.10) a sharp peak is observed in the differential conductance spectrum at -0.7V as well as a smaller peak very close to the Fermi

energy. A comparison of the total LDOS and the normalized dI/dV signal (shown in Fig. 4.15) show a qualitatively good agreement.

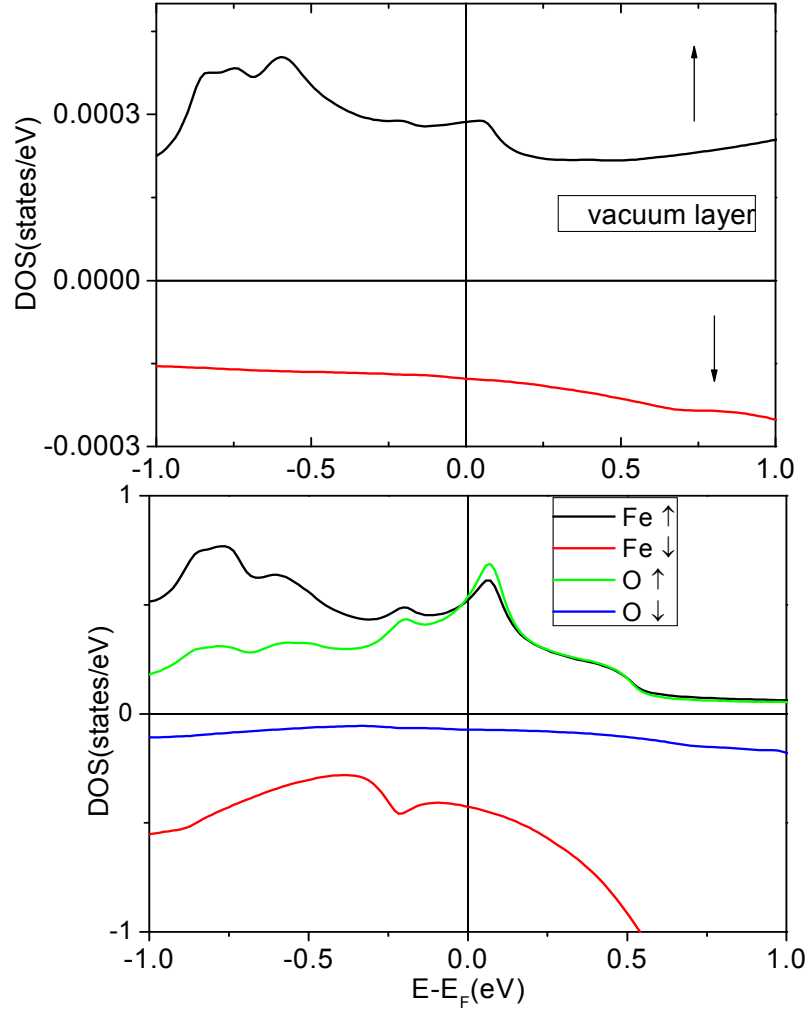


Fig.4.14: Top: DOS in the third vacuum layer from calculations for O/Fe(001). The third vacuum layer lies about 4\AA above the surface. The black and red curves represent the DOS for spin up and spin down electrons, respectively. Bottom: DOS for the surface layer. The spin up (spin down) DOS for Fe and O are indicated.

The calculations show that the peak at -0.6 eV originates from the Fe d_{z^2} orbital. The peak at 0.05 eV originates from oxygen p_z orbital. The bottom curve shows the DOS for spin up and spin down electrons for Fe and O in the surface layer. It shows that there is significant hybridization between the Fe d orbitals with the O p orbitals, mostly in the spin up channel. In particular, the p_z orbital of oxygen

hybridizes with the d_{xy} orbital of iron but due to the planar orientation of the d_{xy} orbital, the main contribution in the vacuum is from the O p_z orbital which is detected as the peak in the DOS at 0.05 eV. Similarly, the d_{z^2} orbital of Fe hybridizes with the p_x and p_y orbitals of O and the main contribution in the DOS in the vacuum comes from the d_{z^2} orbital at -0.6 eV in the spin up channel.

Figure 4.16 shows the spin resolved DOS for the surface plane in wider energy range, displaying the orbital contributions to the features in the DOS and the possible hybridizations between Fe d orbitals with O p orbitals. In the majority spin channel there is strong hybridization between O p_x, p_y orbitals with Fe $d_{x^2-y^2}$ while the p_z orbitals of O hybridize with the d_{xy} orbitals of Fe for states below the Fermi level. Very close to the Fermi level the O p_z orbitals hybridize with the Fe d_{xy} orbitals as already shown in Fig. 4.13. In the minority spin channel the main hybridization occurs between the d_{xy}, d_{z^2} of Fe and p_z orbitals of O for states above the Fermi level.

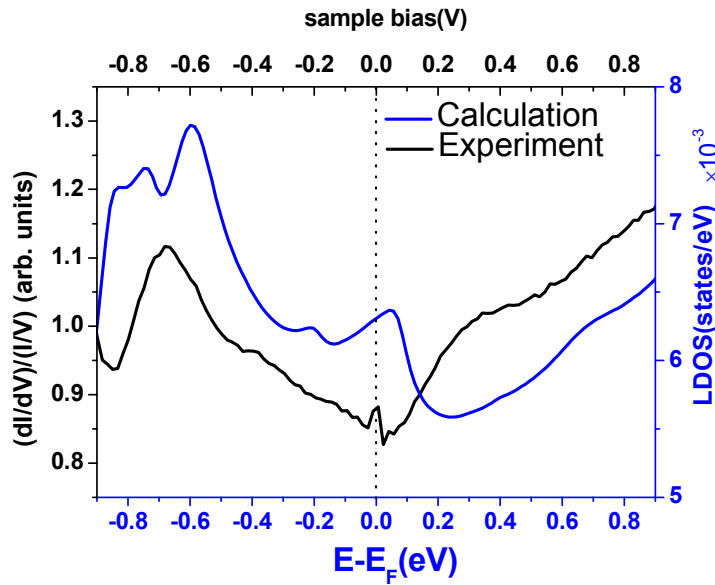


Fig. 4.15: comparison of the total DOS and differential conductivity spectrum of the Fe(001)-p(1×1)O surface.

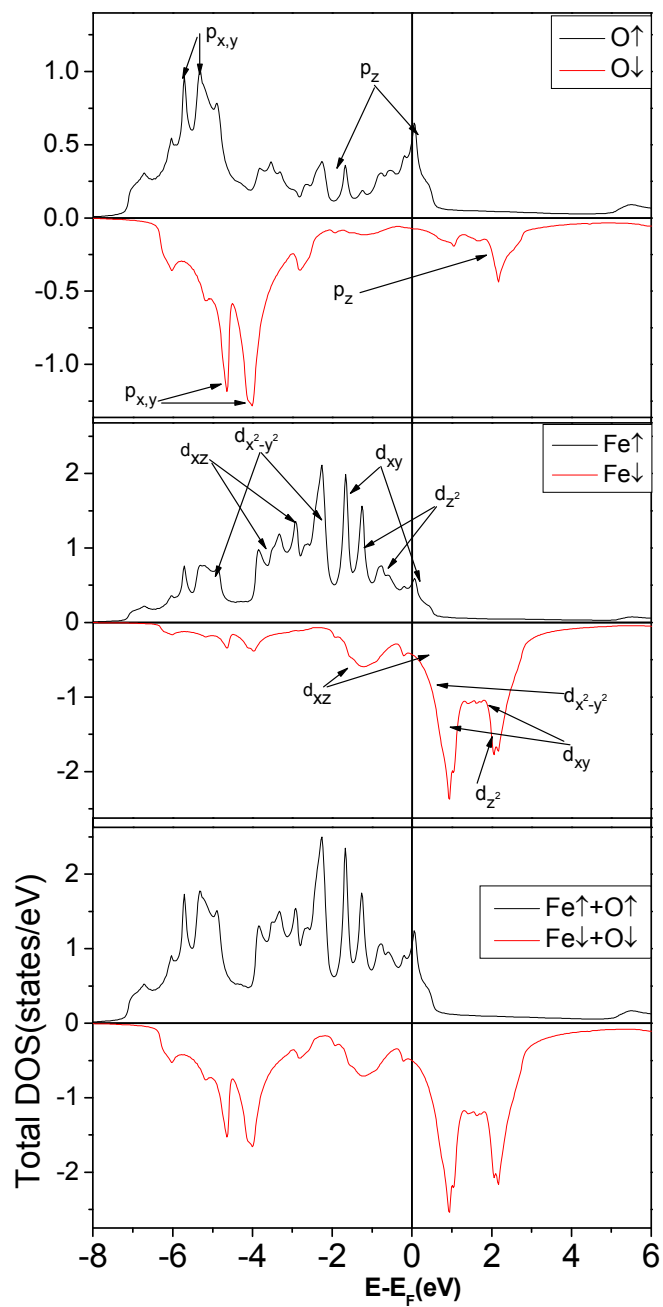


Fig.4.16: Spin resolved DOS for the surface layer for a wider energy range. The oxygen and iron orbitals responsible for the features in the DOS are indicated by arrows.

The difference in the spin signal between the O and Fe sites in the atomically resolved spin images have been evaluated for different voltages (from -1V to +1V). This difference shows a strong dependence on the applied voltage. This is shown in Fig. 4.17. It is small and positive, decreases as the voltages increases and is smaller for more negative voltages with the maximum at 0.1V. No change of sign was observed within the voltage range in the experiment.

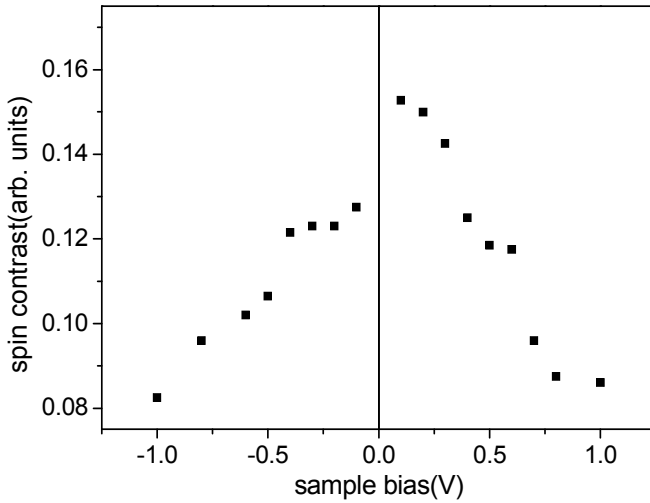


Fig.4.17: Spin contrast as a function of bias voltage from atomically resolved Sp- STM images of Fe(001)-p(1×1)O

The spin polarization in the vacuum region as a function of the energy, obtained from the spin-resolved DOS in Fig.4.14 is shown in Fig.4.18, where the spin polarization is defined as

$$P = \frac{n^{\uparrow} - n^{\downarrow}}{n^{\uparrow} + n^{\downarrow}} \quad (4.1)$$

and $n^{\uparrow(\downarrow)}$ are the spin up (spin down) DOS, respectively. The curve shows a similar trend as in Fig.4.17 except for the maximum which occurs at 0.4 eV in Fig.4.18. It also confirms that the spin polarization on the Fe(001)-p(1×1)O surface is positive. The deviation may be due to effects of tip spin polarization which is often treated as a constant within the Tersoff-Hamann approximation.

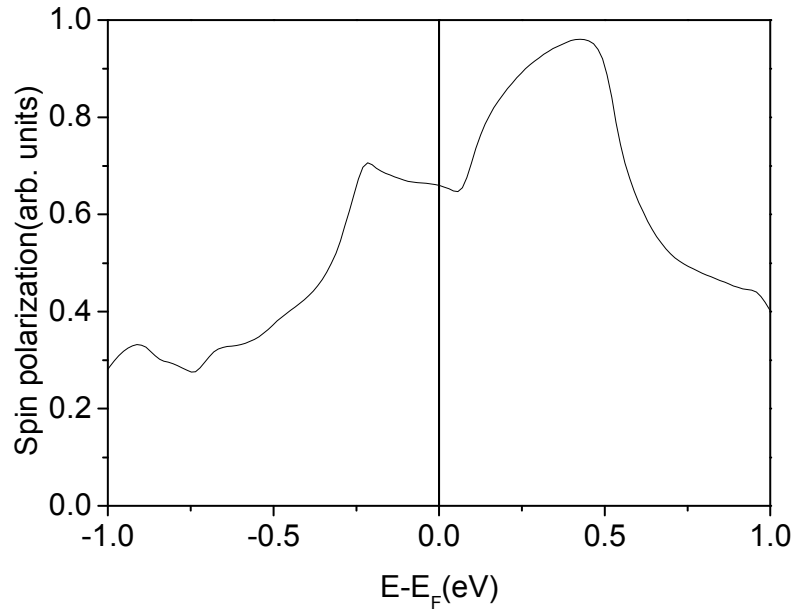


Fig.4.18: Spin polarization as a function of energy, calculated from the DOS in the region above the surface (4Å above the surface)

In summary, it has been shown that with the help of atomically resolved STM data in conjunction with charge density plots, the atomic registry of the Fe(001)-p(1×1)O surface could be identified in real space. The O atoms are imaged as protrusions in the four-fold hollow sites of the surface. The spin-resolved LDOS measured with Sp-STs agrees well with first principle calculations that also show significant hybridization between the O *p* orbitals and Fe *d* orbitals which induces a spin polarization of the oxygen states. The STS measurements were able to detect features at -0.6 eV and 0.05 eV in the majority band of the Fe(001)-p(1×1)O surface that were up to now inaccessible by other conventional spectroscopies like photoemission. The spin polarization of the tunneling current measured from the surface depends on the bias voltage. It is positive and the highest value occurs at 0.1 V, close to the surface feature detected at 0.05 eV on this surface. The positive surface spin polarization is mainly due to the oxygen *p_z* orbitals close to the Fermi level in the majority band.

Chapter 5

Mn Films on Fe(001)-p(1x1)O

Antiferromagnetic thin film materials are widely used in modern magnetic storage devices and will play a major role in next generation storage devices like magnetic random access memories (MRAMs). Understanding the structural as well as magnetic properties of these films, especially when they are in contact with a ferromagnet, is of utmost importance in understanding the properties of the devices incorporating them.

5.1 Properties of Mn on Fe(001)

Bulk manganese has a complex structure and exhibits different phases which show different magnetic behavior depending on the ambient conditions [82]. The stable bulk phase at temperatures up to 1000 K is the complex cubic α -Mn which has 58 atoms per unit cell [83] and shows antiferromagnetism below its Néel temperature of 95K [84]. Between 1000 K and 1370 K cubic β -Mn with 20 atoms per unit cell is the stable phase. Face centered cubic (fcc) γ -Mn exists between 1370 K and 1410 K while body centered cubic (bcc) δ -Mn exists between 1410 K and the melting point 1518 K [85]. Due to these high temperatures it is extremely difficult to characterize bulk Mn materials with the above structures. By choosing an appropriate substrate, different structural phases of Mn can be stabilized at room temperature by epitaxy. On Fe(001), Mn stabilizes in a body centered tetragonal (bct) structure assuming the in-plane lattice constant of the Fe(001) substrate ($a=b=2.866\text{\AA}$) and an out-of-plane lattice constant of $c=3.228\text{\AA}$ [86]. The bct structure persists up to thicknesses between 10 ML to 25 ML depending on the deposition conditions [87] with a resulting structural transition [88, 89] altering the layer-by-layer growth mode to three dimensional growth. Above this thickness there is a transition to α -Mn [90]. The MEED intensity during the growth showed

only two or three maxima following the initial drop in the MEED curve after which it stayed constant until the transition to α -Mn. The disappearance of the MEED oscillations was attributed to a change of growth mode from layer-by-layer to step flow [91]. The films show layerwise antiferromagnetic order [92], i.e. adjacent atomic planes couple antiferromagnetically. In this Chapter, the growth, surface structure and magnetic properties of Mn films grown on Fe(001)-p(1×1)O will be presented and the results compared to that of Mn films grown on the clean Fe(001) surface.

5.2 Growth and structure of Mn on Fe(001)-p(1×1)O

The Mn films are grown by electron beam evaporation of Mn flakes contained in a Mo crucible in a water-cooled evaporator. The growth is monitored by MEED while AES is used to check the composition and the cleanliness of the surface. During deposition the pressure stayed below 5.0×10^{-10} mbar. The substrate was kept at 80°C during the deposition of Mn on Fe(001) and Fe(001)-p(1×1)O, respectively.

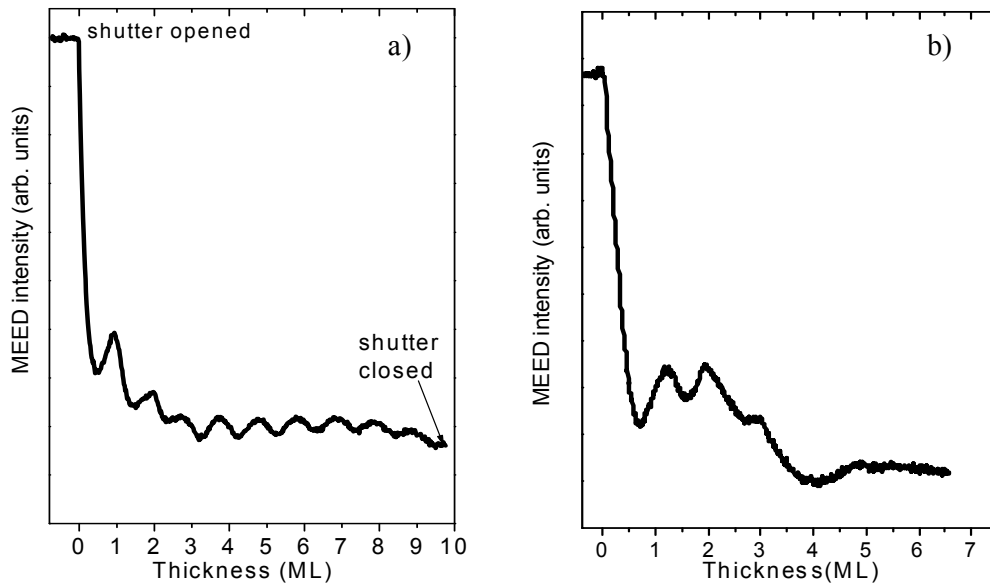


Fig. 5.1: MEED intensity oscillations for (a) Mn on Fe(001)-p(1×1)O and (b) Mn on clean Fe(001) deposited at 80°C .

Typical MEED intensity curves are displayed in Fig. 5.1. The periodic oscillations in the MEED specular spot intensity indicate a layer-by-layer growth mode. There are more oscillations in the MEED curve for the deposition of Mn on Fe(001)-p(1×1)O (Fig. 5.1(a)) than on the clean Fe(001) surface whose MEED curve (Fig. 5.1(b)) shows only two oscillations. One can therefore infer from the MEED intensity oscillations that there is improved layer-by-layer growth on the Fe(001)-p(1×1)O surface compared to the clean Fe(001) surface. Comparison of the Auger peak heights for O, Mn and Fe as a function of Mn thickness (Fig. 5.2) shows that the oxygen intensity is almost invariant. This implies that the oxygen stays on the surface where it acts as a surfactant extending the layer-by-layer growth regime. While the Mn AES signal increases with Mn thickness, the Fe signal decreases almost to zero showing that there is little or no alloying or segregation in the system.

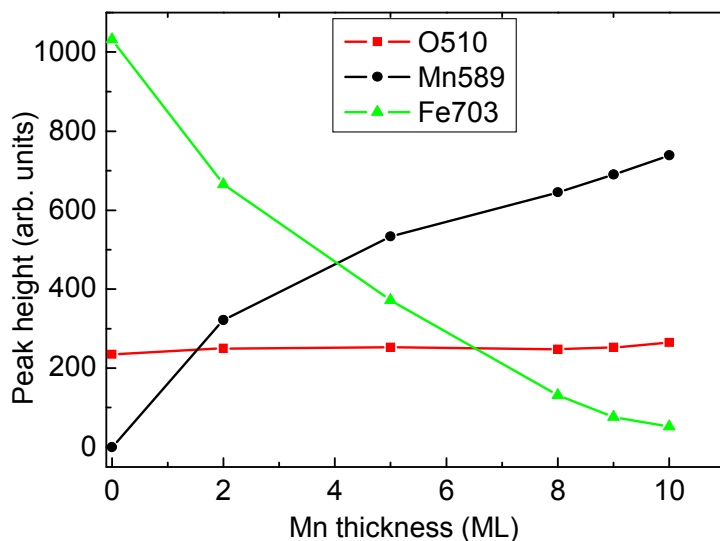


Fig. 5.2: O (510eV), Mn (589eV) and Fe (703eV) Auger peak heights as a function of Mn film thickness on the Fe(001)-p(1×1)O surface.

With the oxygen on the surface, the topmost layer appears more like a two dimensional film of MnO(001). The atomically resolved STM image for 8 ML Mn on Fe(001)-p(1×1)O in Fig. 5.3 shows two terraces, A and B, separated by a monatomic step. Each terrace consists of a square array of protrusions and the

distance between the protrusions is approximately 3.1 Å. This distance is consistent with the 3.14 Å in-plane lattice parameter of MnO(001), which is the separation of Mn atoms on the surface. The protrusions seen in the STM image are most likely Mn atoms. *Ab initio* calculations by Momida and Oguchi [93] for the MnO(001) surface show that the surface presents a rumpled relaxation whereby the O is displaced inward compared to the Mn. The schematic in Fig. 5.3 shows a two dimensional MnO(001) lattice.

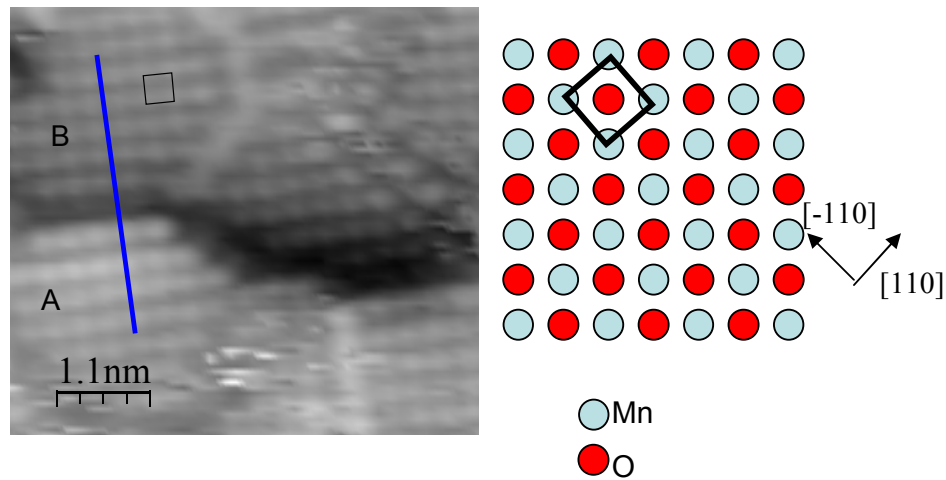


Fig. 5.3: Atomically resolved constant current topography of 8ML Mn on Fe(001)-p(1×1)O. The blue line is a guide to the eye indicating a shift of half a lattice constant in the atomic rows from terrace A to terrace B, typical of bcc metals. The schematic shows a representation of the two-dimensional MnO lattice.

In addition to acting as a surfactant, the oxygen induces a reconstruction on the surface which has been observed for the first time in both LEED and STM. Analysis of the LEED pattern in Fig. 5.4 identifies the reconstruction in matrix notation as $\begin{pmatrix} 6 & 6 \\ 1 & -1 \end{pmatrix}$ consisting of two subpatterns. The unit cell calculated by adopting the lattice of bcc iron has dimensions $a^*=24.32$ Å, $b^*=4.05$ Å. This is indeed observed in atomic resolution STM images (see Fig. 5.5 (a) and (b)), where one observes a network of protrusions rotated 45° with respect to the surface and orthogonal to each other. The reconstruction is oxygen-induced as the surface of

manganese films grown on clean Fe(001) only show a different reconstruction for thicknesses greater than 14 ML, which marks the transition to α -Mn [90]. Possibly the reconstruction lines observed in the STM images could be due to excess oxygen on the surface.

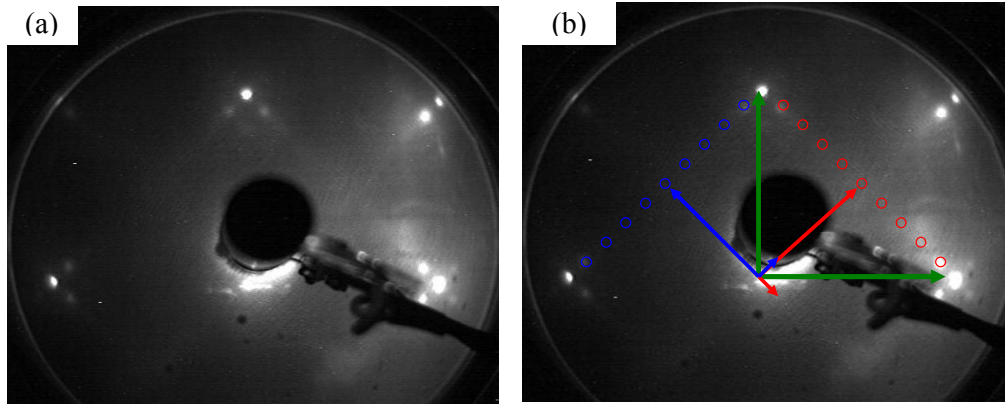


Fig. 5.4: LEED pattern for 9.4 ML Mn on Fe(001)-p(1 \times 1)O taken at 55eV. The blue and red circles in (b) are a guide to the eye for the position of the missing spots after careful analysis of the original LEED pattern shown in (a). The green arrows represent the lattice vectors for the (1 \times 1) substrate basis while the blue and red arrows represent the lattice vectors of the reconstruction.

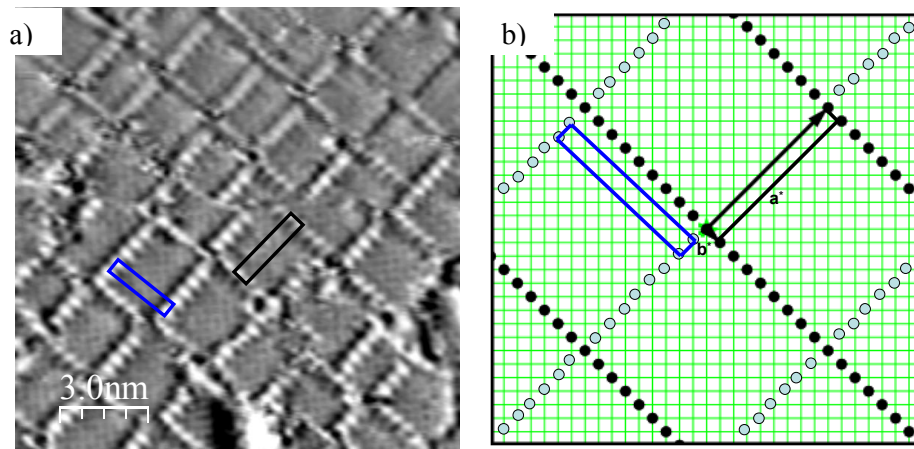


Fig. 5.5: (a) Atomic resolution STM image of 9.4 ML Mn on Fe(001)-p(1 \times 1)O with $I_t = 13.7$ nA, $V_{\text{gap}} = 20$ mV (b) Real space model of the surface obtained from a simulation of the LEED pattern in Fig. 5.4. The blue and black rectangles represent the unit cell of the reconstruction for the two subpatterns, respectively. The small green squares represent the 1 \times 1 substrate unit cell.

5.3 Magnetic structure of Mn films on Fe(001)-p(1×1)O

The topography and corresponding spin signal of 9.4 ML Mn on Fe(001)-p(1×1)O are displayed in Fig 5.6 (a) and (b), respectively. The topography shows large Mn terraces (separated by monatomic steps) containing rectangular islands with rounded edges. Three different Mn layers are exposed to the surface. In the spin image, an alternating black-white contrast is observed between adjacent Mn atomic planes. This is indication of a layerwise antiferromagnetic order similar to that for Mn films on clean Fe(001), i.e. the magnetic moments couple ferromagnetically within one layer and antiferromagnetically between adjacent Mn atomic planes. The presence of the oxygen layer does not disturb the layerwise antiferromagnetic order between adjacent Mn atomic planes, rather, there is an enhancement of the spin contrast compared to the case for Mn on the clean Fe surface [55]. For similar tunneling conditions, the spin contrast is about two times larger for Mn films on Fe(001)-p(1×1)O compared to clean Fe(001) .

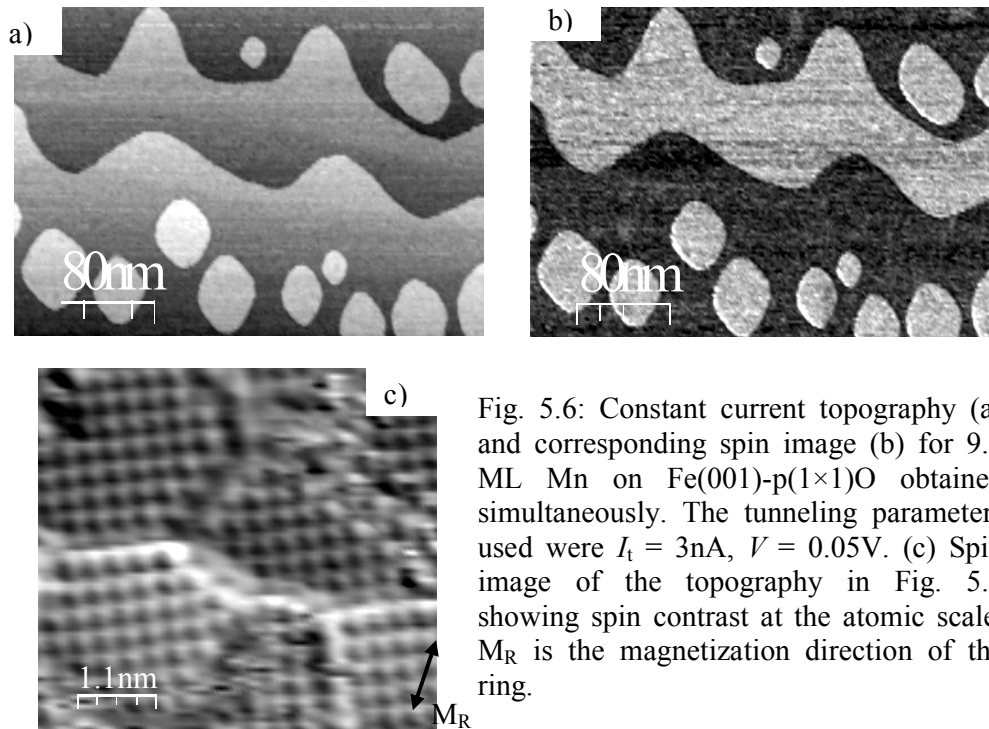


Fig. 5.6: Constant current topography (a) and corresponding spin image (b) for 9.4 ML Mn on Fe(001)-p(1×1)O obtained simultaneously. The tunneling parameters used were $I_t = 3\text{nA}$, $V = 0.05\text{V}$. (c) Spin image of the topography in Fig. 5.3 showing spin contrast at the atomic scale. M_R is the magnetization direction of the ring.

This enhancement of the spin contrast can be attributed to an increased tunneling magnetoresistance (TMR) in the presence of oxygen on the surface. There is a contribution to the spin-polarized tunneling current from the oxygen p-states which become spin-polarized due to hybridization with Mn 3d-states [94, 95]. Fig. 5.6 (c) shows atomically resolved spin image of adjacent Mn atomic layers where the spin contrast is clearly visible at the atomic scale. The atoms on the upper terrace appear much brighter than those on the lower terrace, meaning their moments are opposite to the moment of the atoms on the lower terrace.

5.3.1 Topologically-induced magnetic frustrations

Where the Mn film overgrows a substrate Fe step, the layerwise antiferromagnetic order is interrupted. The presence of the Fe step causes n Mn layers to grow on the upper side while $n+1$ layers grow on the lower side of the step edge. The vertical lattice mismatch between body-centered tetragonal (bct) Mn and bcc Fe leads to the formation of subatomic steps on the Mn film surface at the position of the Fe step. This has consequences on the magnetic order in the film. Since the moments on both sides of the step edge are aligned in the same direction by the Fe substrate, an ideal layerwise antiferromagnetic order is not possible around the step edge. This leads to magnetic frustrations, as the spin polarizations of the Mn layers that meet at such steps are opposite [54, 56], a situation similar to a 180° domain wall. The situation is shown in Fig. 5.8 for the topography (a) and corresponding spin signal (c) of 5 ML Mn overgrowing a monatomic step on the Fe(001)-p(1×1)O substrate. An iron step can be seen at the position indicated by the black arrows in the topography. There is a thickness difference of one ML across the buried Fe step. In the spin signal there is the usual layerwise magnetic contrast between adjacent Mn layers separated by a monatomic step to the right of the image, but in addition, along the buried Fe step (indicated by the arrows to the left of the image) a reversal of the spin contrast is observed. The line profile shown in Fig 5.8 (b) is taken along the blue rectangle in Fig. 5.8 (a). It represents the average of about 25 lines scans. The line shows a step of monatomic height, roughly 1.6 \AA between adjacent Mn layers, and a step of subatomic height (0.3 \AA) at the position of the underlying Fe step, which arises as a result of the lattice

mismatch between Mn and Fe. Figure 5.8 (d) shows the line profile across the frustrated region along the green rectangle in Fig 5.8 (c). It represents the average of 40 different line scans. The average line profile across the frustrated region for a film of thickness 6 ML (not shown) is presented in Fig 5.8 (e). The film thickness and the corresponding width of the frustrated regions are indicated in the figures. To determine the width of such frustrated regions the line profile across the region is fitted to the standard profile of a 180° domain wall [96]. For a one-dimensional 180° domain wall, neglecting the stray field and considering only the exchange interaction and the magneto-crystalline anisotropy, the profile across the wall can be approximated by a *tanh*-function [97]

$$m(x) \propto \tanh(x/w) \quad (5.1)$$

where $m(x)$ is the projection of the magnetization along a direction perpendicular to the domain wall, and the domain wall width, $2w$ is defined as shown in Fig. 5.7 by the intersections of the tangent at $m(0)$ with the saturation lines.

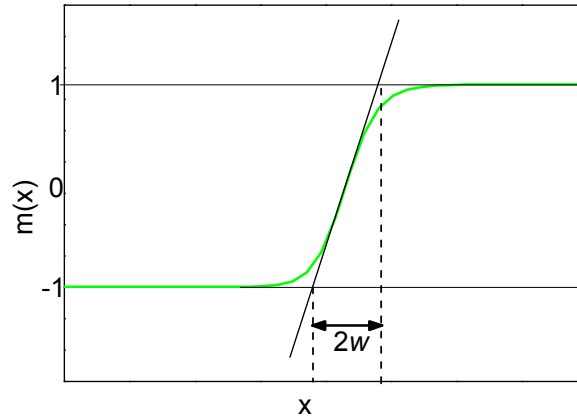


Fig. 5.7: Wall profile for a one-dimensional 180° domain wall modeled with the *tanh*-function in equation (5.1).

The green curves in Fig 5.8 (d) and (e) are the fits of the line profiles across the frustrated region with a *tanh*-function for the 5 ML and 6 ML Mn films, respectively. The calculated wall widths are 3.1 ± 0.1 nm and 4.0 ± 0.1 nm for the 5 ML and 6 ML films, respectively. Though we could not perform a systematic thickness dependence of the width of the frustrated region (not in all cases could we obtain films with buried Fe steps visible on the surface), we observe that the

width of the frustrated region obtained in our experiment are wider compared to those for Mn films on clean Fe for similar film thickness. For 5.5 ML Mn on clean Fe(001) the measured width of the frustrated region is 1.6 ± 0.3 nm [54]. This difference may be due to some oxygen at the buried step edge which could reduce the pinning of the Mn moments or modify the exchange within the frustrated region. The presence of some oxygen at the buried step edge causes frustration to be less localized compared to the case without any oxygen. This would result in a wider width of the frustrated region as schematically drawn in Fig. 5.9.

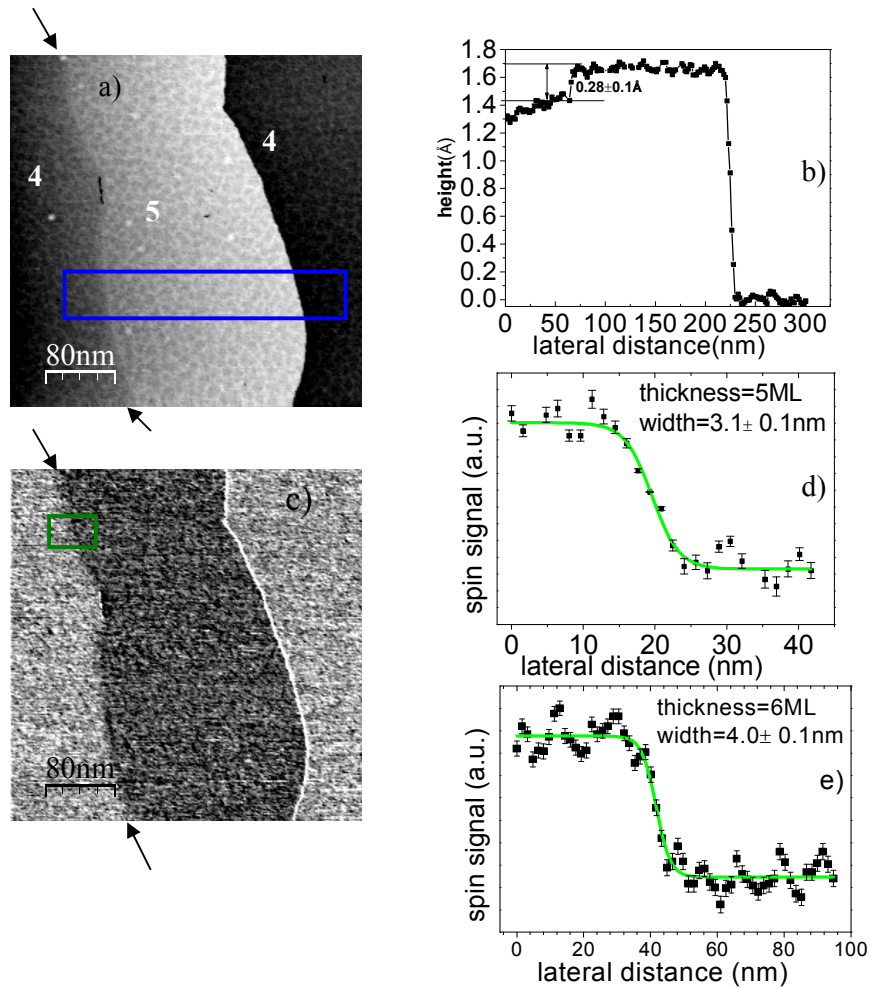


Fig. 5.8: (a) Topography of 5ML Mn on Fe(001)-p(1×1)O showing a buried Fe step indicated by the arrows. The numbers indicate the layer height. (b) Line scan taken along the blue rectangle in (a). (c) Spin image for the corresponding topography in (a) showing a frustrated region across the buried Fe step. (d) Line scan across the frustrated region. The green curve is a fit to the profile using a *tanh* function. (e) Line profile across the frustrated region of a 6ML Mn film.

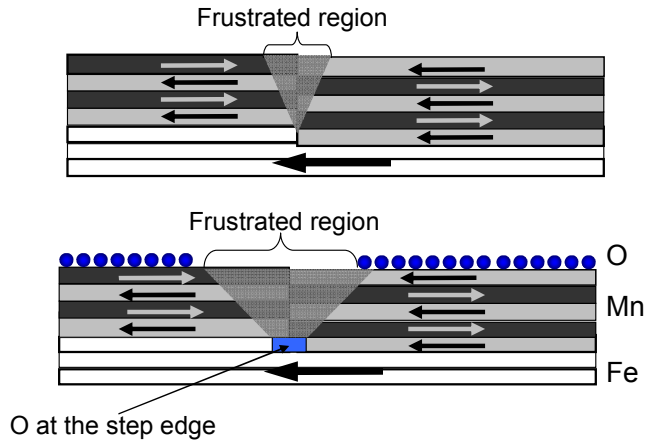


Fig.5.9: Top: Schematic of step-induced frustration in Mn on Fe(001). The frustration is localized at the step edge
Bottom: The frustration becomes less localized due to some O at the step edge leading to a wider frustrated region

Nevertheless, the trend that in thicker Mn films the frustrated regions at the surface are wider is also found for Mn films grown with Oxygen as a surfactant.

In the atomically resolved topography of Fig. 5.10(a), the reconstruction mesh does not seem to follow a particular pattern but rather consists of lines that run along $\langle 110 \rangle$ directions. As stated before, this reconstruction results from excess oxygen on the surface. Since the direction of magnetization of the ring is well-defined (along the $[100]$ direction of the whisker) the spin contrast represents difference in orientation of the moments with respect to this direction. On a single terrace, assuming that the moments point in same direction, a difference in intensity in the spin signal can result from a difference in the magnitude of the local moments. In the spin image in Fig. 5.10 (b) there is a difference in the intensity of the spin signal along the reconstruction lines, higher along the $[-110]$ direction compared to the $[110]$ direction. This suggests that the magnitudes of the induced moments on the oxygen atoms along the reconstruction lines are different in these directions.

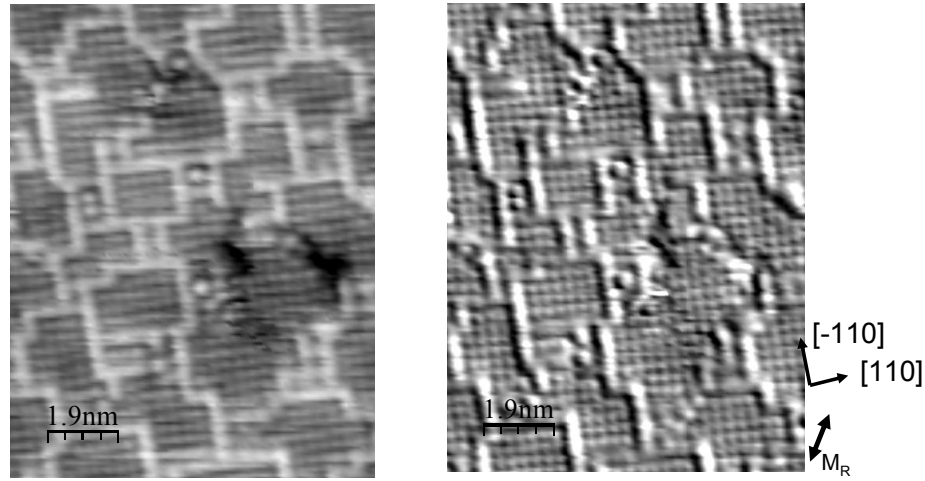


Fig. 5.10: Atomically resolved topography (a) and corresponding spin image (b) of 8ML Mn on Fe(001)-p(1×1)O taken at $I_t = 40\text{nA}$, $V_{\text{gap}} = 20\text{mV}$. M_R denotes the direction of magnetization of the ring.

5.3.2 Voltage dependence of the spin contrast

The variation of the spin contrast as a function of the sample bias is shown in Fig. 5.11. A spin contrast was obtained for the whole range of voltages (-1 V to +1 V) used in the experiment. The spin contrast increases with decreasing voltage for positive sample bias voltage with the maximum spin contrast observed around 0.1V. A change of sign of the contrast occurs at -0.4 V while for the case of Mn on clean Fe(001) the change of sign occurs at -0.2V [55]. This shift is as a result of the enhanced spin contrast observed on the Fe(001)-p(1×1)O surface. The shape of the spin contrast as a function of sample bias shows a similar behavior as for Mn on Fe(001). *Ab initio* calculations on the Mn/Fe(001) system showed that the shape of the spin contrast as a function of bias voltage depends on the Fe bulk bands: e.g., nearly free electrons [55]. The same bulk bands can be used here to explain the similarity in the behavior of the spin contrast for Mn/Fe(001)-p(1×1)O and Mn/Fe(001). The insets in Fig. 5.11 show the spin images acquired at -0.5V and

+0.5V, respectively, where the change of sign in the spin contrast shows up as a reversal of the contrast in the spin images.

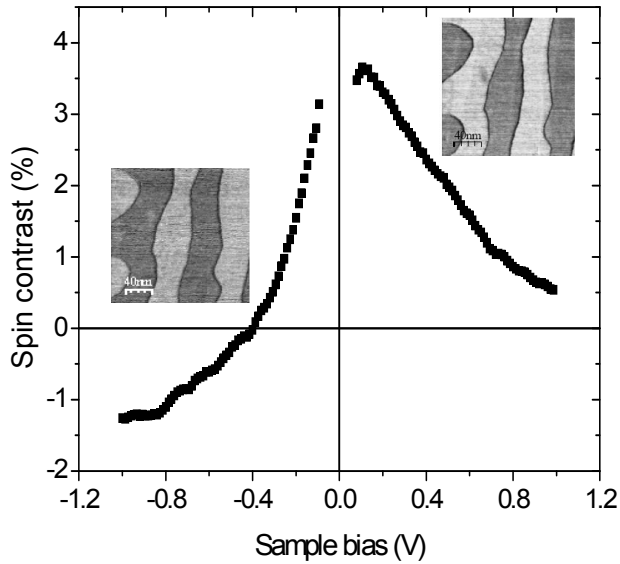


Fig. 5.11: Variation of magnetic contrast as a function of sample bias voltage for 7ML Mn on Fe(001)-p(1×1)O. The insets show the spin images at -0.5V and +0.5V respectively. In the experiment, the voltage was ramped from -1V to -0.05V and from +1V to +0.05V with the feedback loop on.

Scanning tunneling spectroscopy measurements have been performed on the 8ML Mn film using a ferromagnetic ring electrode as the probe tip. In the experiment, the tip was stabilized with a tunneling current of 1 nA and a bias voltage of -1V. The differential conductivity dI/dV was measured directly by modulating the bias voltage with a 30mV signal at 6.5 kHz and detecting the resulting changes in the differential conductivity with a phase-sensitive lock-in amplifier. The measurements were performed on a single terrace and the magnetization of the ring was not switched during the process. The normalized differential conductance spectrum is presented in Fig. 5.12. A peak can be seen around -0.7V. Since the differential conductance is proportional to the local density of states, it means a bulk band edge or a surface state may be present at this voltage. For Mn films deposited on clean Fe(001), Yamada *et al.* [56] observed a pronounced peak at +0.8V and a smaller peak at -0.5 V. In their calculations of the band structure of Mn films on Fe(001), Yamada *et al.* [56] found that the peak at

+0.8 V is caused by two surface states at 0.25 eV and 0.5 eV. The absence of this peak in our experiment is probably caused by the influence of oxygen on the above mentioned surface states. The peak observed at -0.7 V is close to the one observed at -0.5V in ref. [56]. This feature is not much influenced by oxygen and is most likely not a surface state.

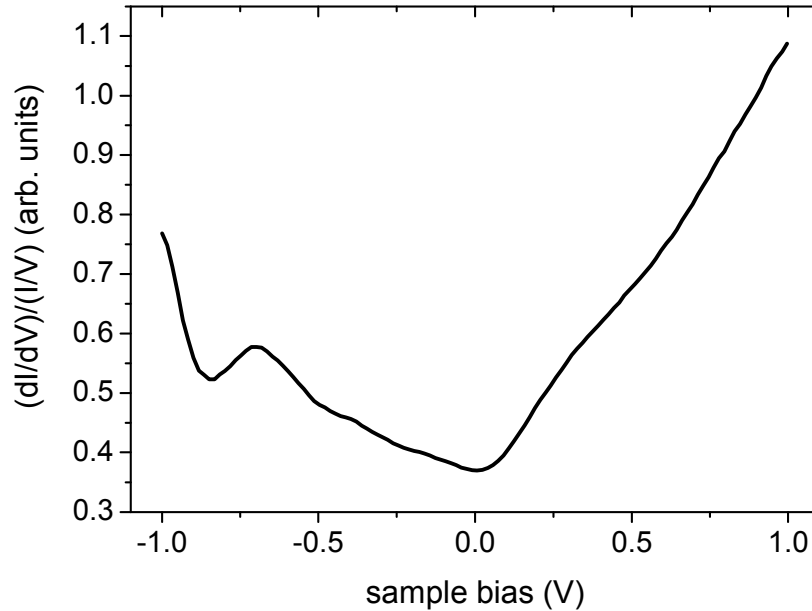


Fig. 5.12: Normalized dI/dV spectra for 8 ML Mn of Fe(001)-p(1x1)O using a ferromagnetic ring electrode

Summary

In this Chapter, it has been shown that the growth of Mn can be improved by growing on Fe(001)-p(1×1)O, where the O acts as a surfactant during the growth process. The Mn films still show layerwise antiferromagnetic order similar to films grown on clean Fe(001) but with an enhanced spin contrast observed between adjacent atomic planes. This enhancement of the spin contrast is attributed to an increase in the TMR for the oxygen covered surface. There is a contribution to the spin-polarized tunneling current from the oxygen p-states which become spin-

polarized due to hybridization with Mn 3d-states. In addition, the voltage dependence of the spin contrast show a similar trend as for Mn films grown on clean Fe(001). Magnetic frustrations are observed on the surface where the film overgrows a buried substrate step edge. The frustrated regions observed here are wider compared to those observed for Mn films on clean Fe. This is attributed to the presence of some oxygen at the buried step edge which causes the frustration to be less localized. The evidence of some oxygen at the step edge on Fe(001)- $p(1\times 1)O$ can be seen in Fig. 4.3(a).

Chapter 6

Mn on Cu₃Au(100)

Apart from having different complex phases in the bulk, Mn also possesses the largest atomic magnetic moment among the 3d metals (about 5 μ_B). Its magnetic properties have thus attracted a lot of attention in recent years especially with the advent of modern deposition techniques whereby different structural phases could be stabilized by epitaxy on well-chosen substrates. In this Chapter the magnetic properties of face-centered tetragonal (fct) Mn grown on Cu₃Au(100) will be studied using spin-polarized STM.

6.1 Growth of Mn on Cu₃Au(100)

The ordered Cu₃Au(100) crystal has a L1₂ structure below 630K [98] with alternating planes of CuAu and Cu perpendicular to the $\langle 100 \rangle$ directions. It is composed of four interpenetrating simple cubic sublattices located at $r_1=(0,0,0)$, $r_2=(1/2,1/2,0)$, $r_3=(1/2,0,1/2)$ and $r_4=(0,1/2,1/2)$ [99] (see Fig. 6.1). With a lattice constant of $a_0=3.75\text{\AA}$ [100], the misfit with fcc Mn is quite small ($\sim 0.6\%$) enabling Mn to grow pseudomorphically on the surface.

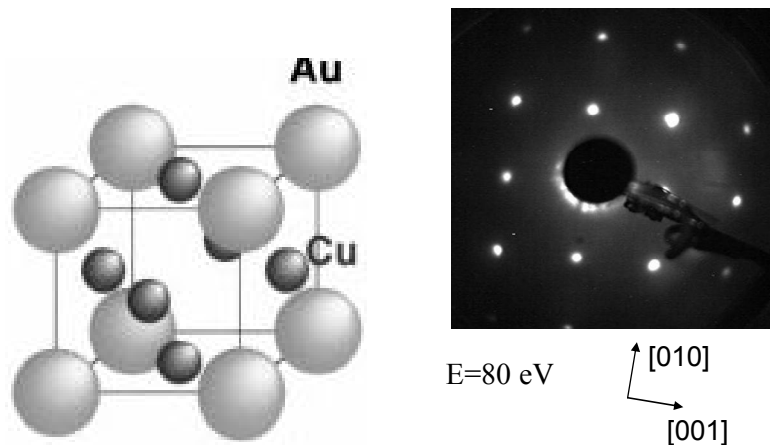


Fig. 6.1: Ordered structure of Cu₃Au(100) showing the chemical ordering at the surface. The LEED pattern on the right shows the $c(2 \times 2)$ surface after cycles of Ar⁺ sputtering and annealing as described in the text. The orientation of the crystal is indicated by the labels on LEED pattern.

The Cu_3Au substrate is prepared by cycles of Ar ion bombardment and annealing after loading into the preparation chamber. Initially, the substrate is sputtered with 2.0 keV Ar ions for several hours followed by annealing for approximately 10 min at 750K and moderate annealing at 525K for about 30 min. This process was repeated until the AES showed no traces of oxygen or carbon and a sharp $c(2 \times 2)$ LEED pattern (see Fig. 6.1) characteristic of the ordered $\text{Cu}_3\text{Au}(100)$ surface was observed.

Lin *et al.* [101] have studied the growth of Mn layers on $\text{Cu}_3\text{Au}(100)$ at room temperature and at low temperature. Using MEED, it was established that at room temperature the growth proceeds layer-by-layer up to 6-7 ML followed by step flow growth mode. It was also shown by LEED-I(V) measurements that the films grown at room temperature undergo a structural transition from fcc to fct between 12-14 ML. We have grown 21 ML Mn on $\text{Cu}_3\text{Au}(100)$ at room temperature. The choice of this thickness is based on the fact that exchange bias was observed for the system 21ML Fe / 14ML Mn / $\text{Cu}_3\text{Au}(100)$ [101] with a blocking temperature of up to 280K, which is an indirect indication of an antiferromagnetic structure for the Mn films. It is thus expected that Mn films of up to 21ML on $\text{Cu}_3\text{Au}(100)$ would have an antiferromagnetic structure with Néel temperature higher than room temperature, hence possible to investigate in real space with our room temperature spin-polarized STM.

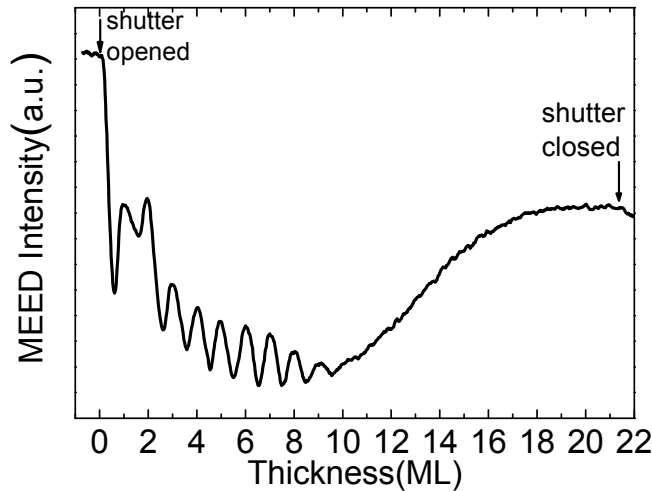


Fig. 6.2: MEED oscillations during the deposition of 21 ML Mn on $\text{Cu}_3\text{Au}(100)$. The oscillations persist up to 9ML after which the intensity increases monotonically, indicating a change of growth mode from layer-by-layer to step flow.

The MEED intensity oscillations for 21 ML Mn / Cu₃Au(100) is shown in Fig. 6.2. The periodic oscillations of the specular beam intensity signify layer-by-layer growth. In this case the oscillations persist up to 9 ML after which there is a monotonic increase in the intensity, implying a possible change of growth mode from layer-by-layer to step flow mode.

6.1.1 Surface structure of Mn films on Cu₃Au(100)

The constant current STM image of a 21 ML Mn film on Cu₃Au(100) in Fig. 6.3 shows large terraces of several hundred nanometers wide with a pattern which consists of grid lines running approximately along the $\langle 100 \rangle$ directions. The almost rectangular units have side lengths of approximately 15 nm to 20 nm and heights about 1.0 Å. A similar tartan pattern was observed for Fe films grown on Cu₃Au(100) [102].

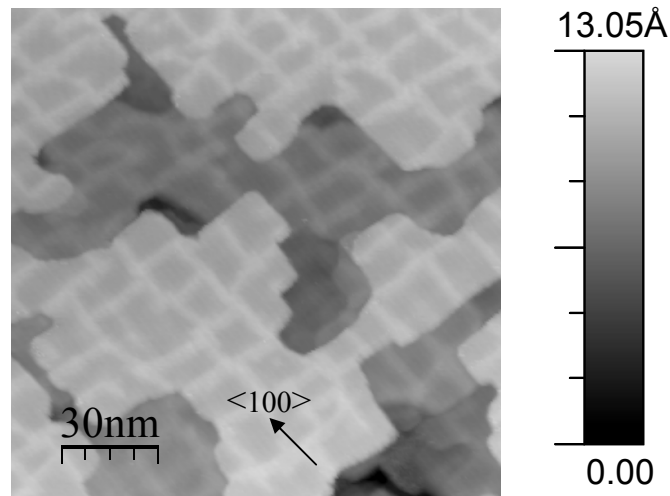


Fig. 6.3: Constant current topography of 21 ML Mn on Cu₃Au(100) acquired at $I=4$ nA, $V=0.11$ V

The pattern results from defects induced during the structural transition.

For smaller film thickness the Mn grows assuming the structure of the Cu₃Au(100) substrate. At larger thickness, due to the lattice mismatch between bulk Mn ($a = 3.796$ Å, $c = 3.59$ Å [103]) and Cu₃Au(100) ($a = 3.75$ Å [100]) the Mn film undergoes a tetragonal distortion in the direction of the surface normal. This

induces an in-plane relaxation that causes the formation of the dislocation pattern on the surface [101].

6.2 Magnetic order of Mn films on Cu₃Au(100)

The topography and corresponding spin signal of a 21 ML Mn film on Cu₃Au(100) is shown in Fig. 6.4. The dislocation pattern described in section 6.1.1 is still observed. Using line scans we can determine the relative height between layers in terms of monatomic height in the topography. The average line profile taken along the rectangle in Fig. 6.4 (a) is shown in Fig. 6.4 (c). The relative height difference between the layers in the topography is indicated in the line profile. It is approximately 3 atomic layers (if we consider the single layer height as 1.8 Å [101]).

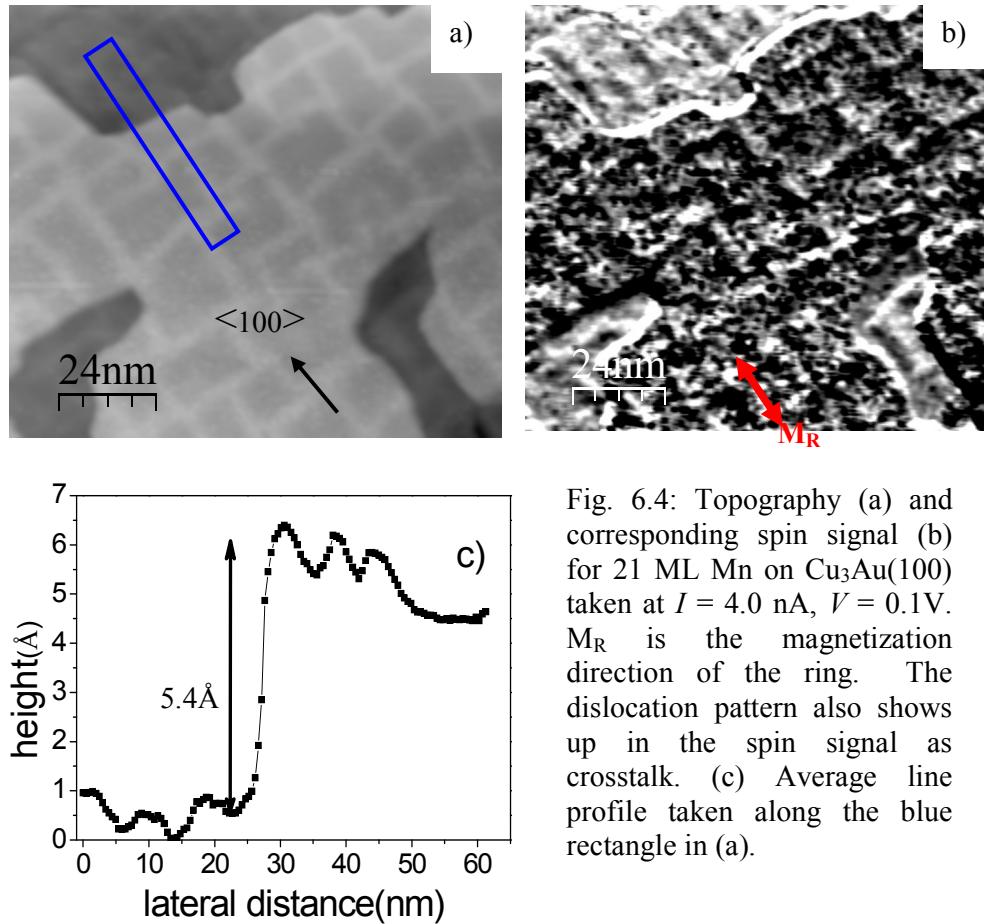


Fig. 6.4: Topography (a) and corresponding spin signal (b) for 21 ML Mn on Cu₃Au(100) taken at $I = 4.0$ nA, $V = 0.1$ V. M_R is the magnetization direction of the ring. The dislocation pattern also shows up in the spin signal as crosstalk. (c) Average line profile taken along the blue rectangle in (a).

In the spin image shown in Fig 6.4 (b), a contrast is observed between Mn planes three monolayers apart i.e. between even and odd layers. This agrees with a layerwise antiferromagnetic order within this region of the film. Large contrasts are also observed around the step edges of the Mn film in the spin signal. This artifact induced by the STM operation is not of magnetic origin but is caused by nonperpendicular tunneling between the ring and the sample at the high step edge or may be due to the finite response time of the feedback loop.

For an ideal layerwise antiferromagnet, the spin signal should alternate between even and odd layers. In our experiments for 21 ML Mn / Cu₃Au(100), this was not always the case, as a deviation from the ideal layerwise antiferromagnetic order was observed in some cases. In the situation depicted in Fig. 6.5, a contrast is observed on Mn planes separated by an even number of layers as seen in the regions marked 3 and 5 in the lower part of Fig. 6.5 (b), or no contrast between layers separated by one ML as in the regions marked 3 and 4 around the middle of the same figure. The separation between Mn atomic planes is indicated by the numbers on the figures (the layer separation was obtained from line scans not shown here). One also observes a contrast in some areas where the layer height is the same as in the regions marked 3 in the upper part of Fig. 6.5 (b). The above observations suggest that there exist an antiferromagnetic domain boundary within the film as indicated by the blue line in the spin image. Such domains may result from the coalescence of islands of different thicknesses as the film grows thicker. The scenario is depicted schematically in Fig. 6.5 (c), where the arrows indicate the direction of magnetization in the different Mn layers and the domain boundary is in the middle. In the initial growth stage of the film at room temperature, there is an absence of long range magnetic order since the Néel temperature is lower than the growth temperature. As the film grows thicker its Néel temperature increases above the growth temperature and the film undergoes a transition to the antiferromagnetic state. During this transition stage there is the tendency to form antiferromagnetic domains within the film.

The deviation from the ideal layerwise antiferromagnetic order is thought to come from local anisotropies due to the surface topography. This might result from

the dislocation pattern which forms as a consequence of the tetragonal distortion during the fcc to fct phase transition.

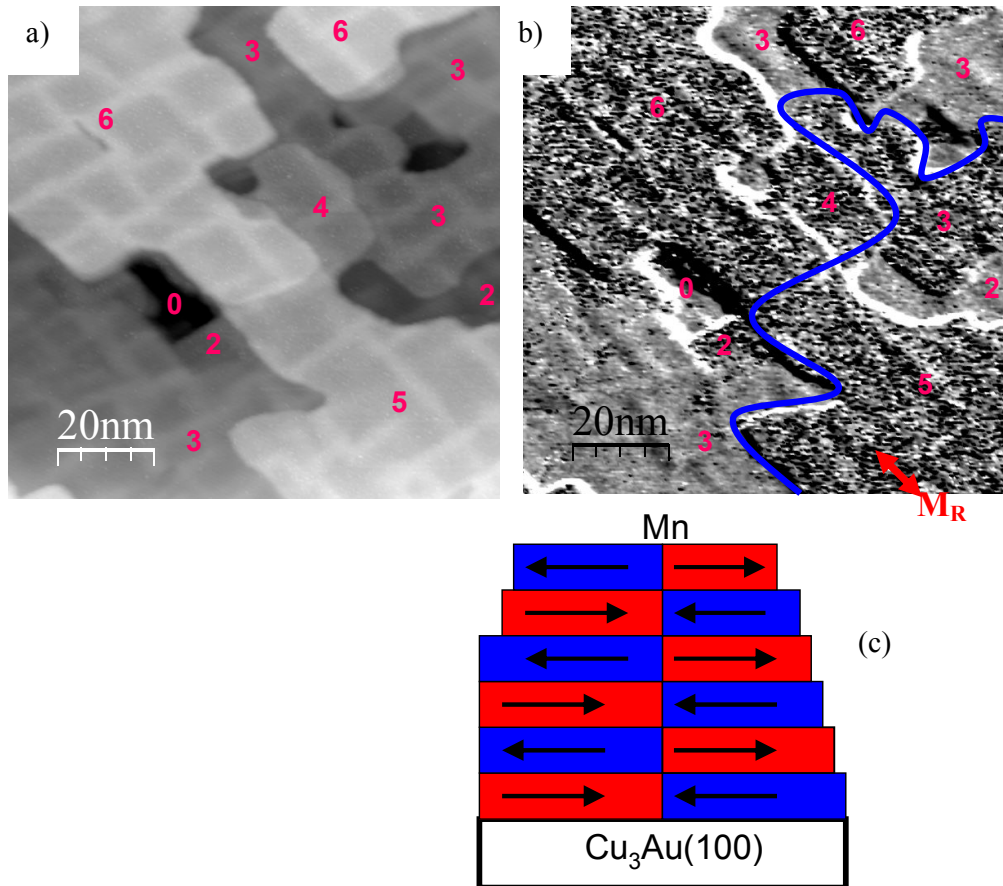


Fig. 6.5: (a) Topography of 21 ML Mn on $Cu_3Au(100)$. The numbers in the figure indicate the number of layers between Mn atomic planes. (b) Spin signal for the topography in (a). The blue line indicates possible antiferromagnetic domain wall in the film. M_R is the direction of magnetization of the ring. The tunneling parameters used were $I = 4.0$ nA, $V = 0.05$ V. (c) Schematic of the possible scenario that leads to formation of the antiferromagnetic domains observed in (b).

In the case for Mn on Fe(001) or Fe(001)-p(1×1)O with the unidirectional magnetic anisotropy provided by the underlying iron whisker, only two intensities are detected in the spin signal representing two unique in-plane orientations of the Mn moments (parallel or antiparallel to the Fe direction). For Mn on $Cu_3Au(100)$,

however, there should exist four unique in-plane orientations of the Mn local magnetic moments due to the four-fold cubic symmetry of the $\text{Cu}_3\text{Au}(100)$ surface. Since SP-STM is sensitive to the projection of the sample surface magnetization onto the tip magnetization, one should observe four different contrasts in the spin image which represent two degenerate domains of the topological antiferromagnetic order with orientations perpendicular to each other [104, 105]. The situation is depicted schematically in Fig. 6.6, where M_t , M_{S1} , M_{S2} , denote the magnetization of the tip, magnetization in domain 1 and magnetization of domain 2 (in the sample), respectively. In the experiment, the magnetization direction of the ring electrode is well-defined i.e. tangential to the periphery of the ring and in the [100] direction of the substrate, indicated by the red arrow M_R in Fig. 6.5 (b).

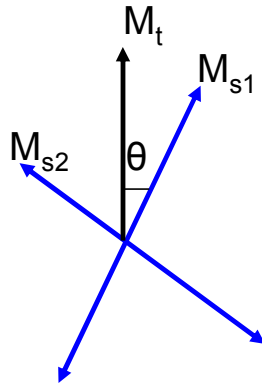


Fig. 6.6: Schematic of the magnetization direction of the tip M_t with respect to two equivalent orthogonal domains M_{S1} and M_{S2} on a surface with four-fold symmetry

Only two contrast levels were observed in the spin images in the experiments as seen in Fig 6.4(b) and Fig. 6.5(b). This implies that either the magnetization direction of the ring was aligned with a 45° angle to the magnetization axis in the domains of topological antiferromagnet, or the areas scanned were not large enough to reveal the two orthogonal domains of topological antiferromagnetic order. The latter can be eliminated, as large area scans of the surface gave the same results. It is more likely that the magnetization direction of the ring is 45° oriented with respect to the spin direction of the antiferromagnetic domains.

6.2.1 $p(2\times 2)$ Superstructure

A closer look at the surface of the Mn films reveal that some terraces the Mn atoms arrange in a $p(2\times 2)$ superstructure. The superstructure is more obvious in the spin signal than in the topographic STM images (Fig. 6.7 (a) and (b)). In Fig. 6.7 (c) and (d) the superstructure is shown in more detail, with the $p(2\times 2)$ unit cell indicated by the blue square. This superstructure is also observed very weakly in LEED (Fig. 6.7 (e)).

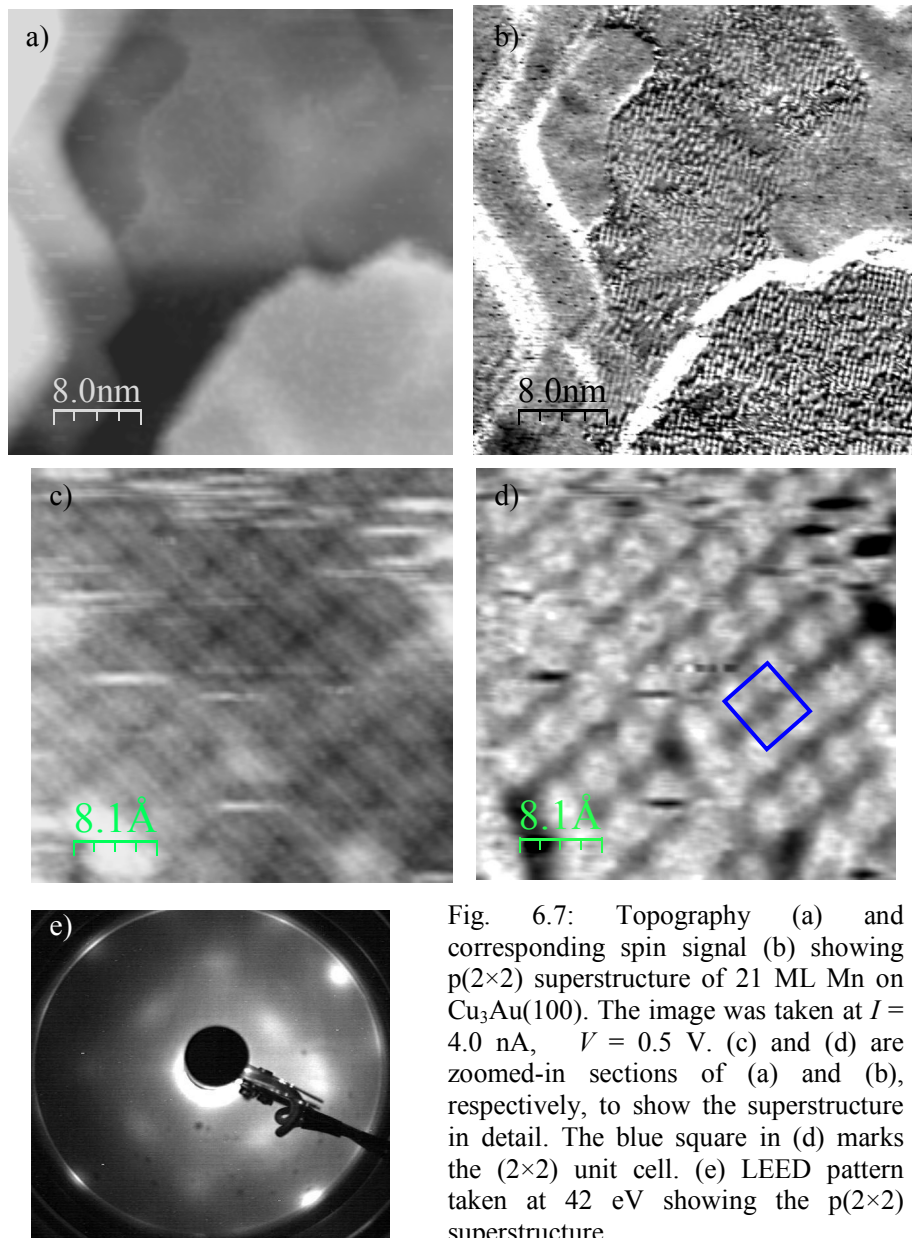


Fig. 6.7: Topography (a) and corresponding spin signal (b) showing $p(2\times 2)$ superstructure of 21 ML Mn on $\text{Cu}_3\text{Au}(100)$. The image was taken at $I = 4.0$ nA, $V = 0.5$ V. (c) and (d) are zoomed-in sections of (a) and (b), respectively, to show the superstructure in detail. The blue square in (d) marks the (2×2) unit cell. (e) LEED pattern taken at 42 eV showing the $p(2\times 2)$ superstructure.

From the theoretical analysis of Krüger *et al.* [106] on the magnetic structures of Mn at the (001) surface, it was found that there is only a tiny energy difference between the $c(2\times 2)$ compensated and $p(2\times 2)$ uncompensated magnetic configurations, with the $c(2\times 2)$ being the most stable configuration. However, surface relaxation and/or reconstruction as well as structural imperfections might overcome this energy difference between these two configurations such that the $p(2\times 2)$ uncompensated becomes the most stable configuration. The structural imperfections in our case for 21 ML Mn on $\text{Cu}_3\text{Au}(100)$ come from the surface relaxation that occur during the formation of the dislocation pattern. The $p(2\times 2)$ reconstruction was observed only on certain terraces, probably the reason why the LEED pattern is weak. The $p(2\times 2)$ uncompensated configuration is thus believed to be the stable magnetic configuration for the case of 21 ML Mn/ $\text{Cu}_3\text{Au}(100)$. Moreover, the tetragonal distortion has been shown theoretically to originate from a directional property of the d-band bonding introduced by the antiferromagnetic ordering in γ -Mn [107, 108] i.e. it is a magnetically induced tetragonal lattice distortion.

Chapter 7

Conclusion

In the first part of this work, the Fe(001)-p(1×1)O surface was studied as well as the effect of the oxygen layer on the magnetism of Mn films grown on this surface. This was done by means of spin-polarized scanning tunneling microscopy operating in the differential magnetic mode at room temperature. By using a soft ferromagnetic material in the form of a ring for the STM electrode, in-plane sensitivity was achieved. With a coil wound around the ring, the magnetization of the ring is switched periodically by applying a high frequency alternating current through the coil. The resulting change in the tunneling current due to this reversal of tip magnetization is detected through a phase sensitive lock-in amplifier. This quantity which is a projection of the sample surface spin polarization onto the magnetization direction of the ring is a purely magnetic signal, separate from the average tunneling current (output from STM feedback loop) which is proportional to the surface topography.

Atomically resolved STM topography images together with theoretical calculations [77] confirm for the first time the surface atomic registry of the Fe(001)-p(1×1)O surface in real space, which had been previously studied in reciprocal space by LEED [74]. The O atoms sit in the four-fold hollow sites on the surface and are imaged as protrusions at these sites in atomically resolved STM. The atomically resolved spin image shows reasonable agreement with spin density contours for the system obtained from theoretical calculations [77], where the maximum spin signal is obtained above the oxygen adsorption sites. The spin polarization of the tunneling current from this surface depends on the applied voltage. It decreases with increasing voltage with the highest value obtained for

+0.1V. Close to point defects (missing O atoms) on the surface the spin signal is enhanced locally. The differential conductance spectrum of the surface obtained from scanning tunneling spectroscopy identified a feature around -0.7 eV and another very close to the Fermi level. *Ab initio* calculations performed using the Koringa-Kohn-Rostoker method reveal that these features results from a hybridization of the oxygen *p*-orbitals with the iron *d*-orbitals. In particular, the positive spin polarization from this surface is mainly due to the presence of oxygen p_z orbitals close to the Fermi level which was detected here for the first time with scanning tunneling spectroscopy.

When Mn was grown on the Fe(001)-p(1×1)O surface, an improvement of the layer-by-layer growth compared to the case on clean Fe(001) was observed. The O was found to play a surfactant role in the growth process. The Sp-STM results revealed that the Mn films show layerwise antiferromagnetic order similar to the case for films on clean Fe(001). The difference in the spin-polarized tunneling current measured between adjacent Mn terraces (spin contrast) showed voltage dependence in the range -1 V to +1 V similar to the case on clean Fe but larger in absolute value. Magnetic frustrated regions were also found on the surface of Mn films on Fe(001)-p(1×1)O. These magnetic frustrations occur where the Mn film overgrows a step of the substrate. The width of the frustrated region for 5 ML and 6 ML Mn films on Fe(001)-p(1×1)O were 3.1 ± 0.1 nm and 4.0 ± 0.1 nm, respectively, much larger than the 1.6 ± 0.3 nm obtained for 5.5 ML Mn on Fe(001) [54]. The presence of some oxygen at the buried step edge causes the magnetic frustration to be less localized compared to the case without oxygen resulting in a wider frustrated region.

In the second part of this study, it was shown directly that 21 ML fct Mn stabilized on Cu₃Au(100) has an uncompensated antiferromagnetic structure using Sp-STM. A constant spin contrast was observed between Mn terraces separated by odd number of layers, indicating a layerwise antiferromagnetic order within the film. In some cases a deviation from the ideal layerwise antiferromagnetic order was found. A p(2×2) superstructure was observed on some terraces on the surface and is thought to be the stable magnetic configuration for 21 ML Mn on Cu₃Au(100).

References

- [1] G.E.Bacon. *Neutron diffraction*. Oxford, 1962.
- [2] Y.Martin and H.K.Wickramasinghe. *Appl. Phys. Lett.* **50**, 1455 (1987).
- [3] L.Abelmann, S.Porthun, M.Haast, C.Lodder, A.Moser, M.E.Best, P.J.A.van Schendel, B.Stiefel, H.J.Hug, G.P.Heydon, A.Farley, S.R.Hoon, T.Pfaffelhuber, R.Proksch, and K.Babcock. *J. Magn. Magn. Mater.* **190**, (1998).
- [4] H.J.Williams, F.G.Foster, and E.A.Wood. *Phys. Rev.* **82**, 119 (1951).
- [5] K.Koike, H.Matsuyama, H.Todokoro, and K.Hayakawa. *Scanning Microscopy* **1**, 31 (1987).
- [6] C.T.Chen, Y.U.Idzerda, H.J.Lin, G.Meigs, A.Chaiken, G.A.Prinz, and G.H.Ho. *Phys. Rev. B* **48**, 642 (1993).
- [7] G.Binnig, H.Rohrer, Ch.Gerber, and E.Weibel. *Phys. Rev. Lett.* **49**, 57 (1982).
- [8] G.Binnig, H.Rohrer, C.Gerber, and E.Weibel. *Appl. Phys. Lett.* **40**, 178 (1982).
- [9] S.Heinze, M.Bode, A.Kubetzka, O.Pietzsch, X.Nie, S.Blugel, and R.Wiesendanger. *Science* **288**, (2000).
- [10] R.Wiesendanger, H.J.Güntherodt, G.Güntherodt, R.J.Gambino, and R.Ruf. *Phys. Rev. Lett.* **65**, 247 (1990).
- [11] S.Ohnishi, A.J.Freeman, and M.Weinert. *Phys. Rev. B* **28**, 6741 (1983).
- [12] E.Yu.Tsymbal, I.I.Oleinik, and D.G.Pettifor. *J. Appl. Phys.* **87**, 5230 (2000).
- [13] E.Vescovo, O.Rader, and C.Carbone. *Phys. Rev. B* **47**, 13051 (1993).
- [14] P.Blonski, A.Kiejna, and J.Hafner. *Surf. Sci* **590**, 88 (2005).
- [15] P.Blonski, A.Kiejna, and J.Hafner. *J. Phys. : Condens Matter* **19**, 096011 (2007).
- [16] R.Bertacco and F.Ciccacci. *Phys. Rev. B* **59**, 4207 (1999).
- [17] P.D.Johnson. *J. Electron. Spectrosc. Relat. Phenom.* **51**, 249 (1990).

- [18] M.Wuttig and X.Liu. *Ultrathin Metal films: Magnetic and Structural Properties*. Springer, 2004.
- [19] J.A.C.Bland and B.Heinrich. *Ultrathin Magnetic structures*. Springer Verlag, Berlin. 1994.
- [20] A.Scholl, M.Liberati, E.Arenholz, H.Ohldag, and J.Stöhr. Phys. Rev. Lett. **92**, 247201 (2004).
- [21] E.C.Stoner. Proc. Roy. Soc. A **54**, 656 (1936).
- [22] V.L.Moruzzi, J.F.Janak, and A.R.Williams. *Calculated electronic Properties of Metals*. Pergamon Press Inc., 1978.
- [23] C.H.Park, B.C.Lee, and J.I.Lee. J. Korean Phys. Soc. **47**, 655 (2005).
- [24] S.Bluegel. Phys. Rev. Lett. **68**, 851 (1992).
- [25] R.L.Fink, G.A.Mulhollan, A.B.Andrews, J.L.Erskine, and G.K.Walters. Phys. Rev. B **45**, 9824 (1992).
- [26] A.Seiler, C.S.Feigerte, J.L.Pena, R.J.Cellotta, and D.T.Pierce. J. Appl. Phys. **57**, 3638 (1985).
- [27] M.Getzlaff, D.Egert, P.Rappolt, M.wilhelm, H.Steidl, G.Baum, and W.Raith. Surf. Sci. **331-333**, 1404 (1995).
- [28] W.Weber, D.Kerkmann, D.Pescia, D.A.Wesner, and G.Güntherodt. Phys. Rev. Lett. **65**, 2058 (1990).
- [29] Z.Gamow. Z. Physik **51**, 204 (1928).
- [30] R.Fowler and L.Nordheim. Proc. Roy. Soc. A **119**, 178 (1928).
- [31] G.Binnig, H.Rohrer, C.Gerber, and E.Weibel. Appl. Phys. Lett. **40**, 178 (1982).
- [32] J.Bardeen. Phys. Rev. Lett. **6**, (1961).
- [33] J.Tersoff and D.R.Hamann. Phys. Rev. Lett. **50**, 1998 (1983).
- [34] J.Tersoff and D.R.Hamann. Phys. Rev. B **31**, 805 (1985).
- [35] M.Jullière. Phys. Lett. A **54**, 225 (1975).
- [36] B.Bhushan and H.Fuchs. *Applied scanning probe methods II: scanning probe microscopy techniques*. Springer, 2006.
- [37] J.Slonczewski. Phys. Lett. B **39**, 6995 (1989).
- [38] M.Johnson and J.Clark. J. Appl. Phys. **67**, 6141 (1990).

- [39] D.T.Pierce. *Physica Scripta* **38**, 291 (1988).
- [40] M.Bode, M.Getzlaff, and R.Wiesendanger. *Phys. Rev. Lett.* **81**, 4256 (1998).
- [41] W.Wulfhekel and J.Kirschner. *Appl. Phys. Lett.* **75**, 1944 (1999).
- [42] H.Yang, A.R.Smith, M.Prikhodko, and W.R.L.Lambrecht. *Phys. Rev. Lett.* **89**, 226101 (2002).
- [43] M.Bode, E.Y.Vedmedenko, K.von Bergmann, A.Kubetzka, P.Ferriani, S.Heinze, and R.Wiesendanger. *Nat Mater* **5**, 477 (2006).
- [44] A.Kubetzka, P.Ferriani, M.Bode, S.Heinze, G.Bihlmayer, K.von Bergmann, O.Pietzsch, S.Blugel, and R.Wiesendanger. *Phys. Rev. Lett.* **94**, 087204 (2005).
- [45] N.Berdunov, S.Murphy, G.Mariotto, and I.V.Shvets. *Phys. Rev. Lett.* **93**, (2004).
- [46] F.Meier, L.Zhou, J.Wiebe, and R.Wiesendanger. *Science* **320**, 82 (2008).
- [47] D.Wortmann, S.Heinze, P.Kurz, G.Bihlmayer, and S.Blügel. *Phys. Rev. Lett.* **86**, 4132 (2001).
- [48] W.Wulfhekel and J.Kirschner. *Annu. Rev. Mater. Res.* **37**, 69 (2007).
- [49] W.Wulfhekel and J.Kirschner. *Appl. Phys. Lett.* **75**, 1944 (1999).
- [50] P.Auger. *Journal de physique et radium* **6**, (1925).
- [51] J.Pendry. *Low energy electron diffraction*. Academic Press, London. 1974.
- [52] Micro-STM. Omikron Vacuumphysik.
- [53] U. Schlickum. Spin polarized scanning tunneling microscopy studies on in-plane magnetization components of thin antiferromagnetic films on Fe(001). 2005. Halle, Martin-Luther-Universität. Ref Type: Thesis/Dissertation
- [54] U.Schlickum, N.Janke-Gilman, W.Wulfhekel, and J.Kirschner. *Phys. Rev. Lett.* **92**, 107203 (2004).
- [55] U.Schlickum, C.L.Gao, W.Wulfhekel, J.Henk, P.Bruno, and J.Kirschner. *Phys. Rev. B* **74**, 54409 (2006).
- [56] T.K.Yamada, M.M.J.Bischoff, G.M.M.Heijnen, T.Mizoguchi, and H.van Kempen. *Phys. Rev. Lett.* **90**, 056803 (2003).
- [57] M.Getzlaff, J.Bansmann, and G.Schoenhense. *J. Magn. Magn. Mater.* **192**, 458 (1999).

- [58] G.Panzner, D.R.Mueller, and T.N.Rhodin. Phys. Rev. B **32**, 3472 (1985).
- [59] C.R.Brundle. Surf. Sci. **66**, 581 (1977).
- [60] C.Brucker and T.N.Rhodin. Surf. Sci. **57**, 523 (1976).
- [61] A.Clarke, N.B.Brookes, P.D.Johnson, M.Weinert, B.Sinković, and N.V.Smith. Phys. Rev. B **41**, 9659 (1990).
- [62] H.Huang and J.Hermanson. Phys. Rev. B **32**, 6312 (1985).
- [63] P.D.Johnson, A.Clarke, N.B.Brookes, S.L.Hulbert, B.Sinkovic, and N.V.Smith. Phys. Rev. Lett. **61**, 2257 (1988).
- [64] Š.Pick. Czech. J. Phys. **47**, 451 (1997).
- [65] R.Wu and A.J.Freeman. Phys. Rev. Lett. **69**, 2867 (1992).
- [66] A.Winkelmann, D.Hartung, H.Engelhard, C.T.Chiang, and J.Kirschner. Rev. Sci. Instrum. **79**, 083303 (2008).
- [67] M.M.J.Bischoff, C.Konvicka, A.J.Quinn, M.Schmid, J.Redinger, R.Podloucky, P.Varga, and H.van Kempen. Phys. Rev. Lett. **86**, (2001).
- [68] K.O.Legg, F.P.Jona, D.W.Jepsen, and P.M.Marcus. J. Phys. C **8**, L492 (1975).
- [69] C.Leygraf and S.Ekelund. Surf. Sci. **40**, 609 (1973).
- [70] Y.Sakisaka, T.Miyano, and M.Onchi. Phys. Rev. B **30**, 6849 (1984).
- [71] G.W.Simmons and D.J.Dwyer. Surf. Sci. **48**, 373 (1975).
- [72] H.Viefhaus and H.J.Grabke. Surf. Sci. **109**, (1981).
- [73] S.R.Chubb and W.E.Pickett. Solid State Commun. **62**, 19 (1987).
- [74] F.P.Jona and P.M.Marcus. Solid State Commun. **64**, 667 (1987).
- [75] M.M.J.Bischoff, T.K.Yamada, C.M.Fang, R.A.de Groot, and H.van Kempen. Phys. Rev. B **68**, 045422 (2003).
- [76] J.A.Stroschio, D.T.Pierce, A.Davies, R.J.Celotta, and M.Weinert. Phys. Rev. Lett. **75**, 2960 (1995).
- [77] R.Wu and A.J.Freeman. J. Mag. Magn. Mater. **127**, 327 (1993).
- [78] E.Yu.Tsymbal, I.I.Oleinik, and D.G.Pettifor. J. Appl. Phys. **87**, 5230 (2000).
- [79] W.Kohn and N.Rostoker. Phys. Rev. **94**, 1111 (1954).

- [80] J.Korringa. *Physica* **13**, 392 (1947).
- [81] G.Kresse and J.Furthmüller. *Comput. Mate. Sci.* **6**, 15 (1996).
- [82] D.Hobbs, J.Hafner, and D.SpiŠák. *Phys. Rev. B* **68**, 014407 (2003).
- [83] A.J.Bradley and J.Thewlis. *Proc. Roy. Soc. A* **115**, 456 (1927).
- [84] R.Tebble and D.Craik. *Magnetic Materials*. Interscience, London. 1969.
- [85] R.W.G.Wyckoff. *Crystal Structures*. Interscience Publishers, New York. 1963.
- [86] S.K.Kim, Y.Tian, M.Montesano, F.Jona, and P.M.Marcus. *Phys. Rev. B* **54**, 5081 (1996).
- [87] S.T.Purcell, M.T.Johnson, N.W.E.McGee, R.Coehoorn, and W.Hoving. *Phys. Rev. B* **45**, 13064 (1992).
- [88] S.Andrieu, M.Finazzi, P.Bauer, H.Fischer, P.Lefevre, A.Traverse, K.Hricovini, G.Krill, and M.Piecuch. *Phys. Rev. B* **57**, 1985 (1998).
- [89] E.C.Passamani, B.Croonenborghs, B.Degroote, and A.Vantomme. *Phys. Rev. B* **67**, 174424 (2003).
- [90] C.L.Gao, U.Schlickum, W.Wulfhekel, and J.Kirschner. *Phys. Rev. Lett.* **98**, 107203 (2007).
- [91] C. L. Gao. Spin structure of antiferromagnetic thin films investigated by spin polarized scanning tunneling microscopy. 2006. Halle, Martin-Luther-Universität.
Ref Type: Thesis/Dissertation
- [92] T.G.Walker and H.Hopster. *Phys. Rev. B* **48**, (1993).
- [93] H.Momida and T.Oguchi. *J. Phys. Soc. Jpn* **72**, 588 (2003).
- [94] S.Andrieu, E.Foy, H.Fischer, M.Alnot, F.Chevrier, G.Krill, and M.Piecuch. *Phys. Rev. B* **58**, 8210 (1998).
- [95] H.Zenai, S.Bouarab, J.Ferrer, and C.Demangeat. *Surf. Sci* **564**, 12 (2004).
- [96] A.Hubert and R.Shäfer. *Magnetic domains: the analysis of magnetic microstructures*. Springer, Berlin. 1998.
- [97] J.Weissenrieder, M.Goethelid, M.Mansson, H.v.Schenck, O.Tjernberg, and U.O.Karlson. *Surf. Sci* **527**, (2003).
- [98] H.Okamoto, D.J.Chakrabarti, D.E.Laughlin, and T.B.Massalski. *Binary Alloy Phase Diagrams*. American Society for Metals, Ohio. 1990.

- [99] H.Dosch and H.Reichert. *Acta Mater.* **48**, 4387 (2000).
- [100] J.D.Donnaym, G.Donnay, E.C.Cox, O.Kennard, and M.V.King. *Crystal Data, Determinative Tables*. American Crystallographic Association, 1963.
- [101] W.C.Lin, T.Y.Chen, L.C.Lin, B.Y.Wang, Y.W.Liao, K.-J.Song, and M.-T.Lin. *Phys. Rev. B* **75**, 054419 (2007).
- [102] M.-T.Lin, J.Shen, W.Kuch, H.Jenniches, C.M.Schneider, and J.Kirschner. *Surf. Sci* **410**, 290 (1998).
- [103] Y.Endoh and Y.Ishikawa. *J. Phys. Soc. Jpn.* **30**, 1614 (1971).
- [104] T.Kawagoe, Y.Iguchi, T.K.Yamada, Y.Suzuki, K.Koike, and S.Suga. *Phys. Rev. B* **71**, 014427 (2005).
- [105] R.Ravlic', M.Bode, A.Kubetzka, and R.Wiesendanger. *Phys. Rev. B* **67**, 17441 (2003).
- [106] P.Krüger, O.Elmouhssine, C.Demangeat, and J.C.Parlebas. *Phys. Rev. B* **54**, 6393 (1996).
- [107] T.Oguchi and A.J.Freeman. *J. Mag. Magn. Mater.* **46**, L1 (1984).
- [108] H.Duschanek and K.Schwarz. *Physica B* **161**, 139 (1989).

Acknowledgements

I would first of all like to express my sincere thanks to Professor Jürgen Kirschner for giving me the opportunity to carry out my research in his department at the Max Planck Institute of Microstructure Physics. His vast knowledge and constant advice was of immense help to me during the past three years and his patience gave me the courage to carry on even in the most difficult moments.

I am equally indebted to Professor Wulf Wulfhekel for all his support and guidance. His expertise in spin-polarized scanning tunneling microscopy helped me understand the details of the experiments and results. His most efficient suggestions were crucial to my work.

Special thanks to Dr. Chunlei Gao for teaching me many tricks in running the experiments and help in interpreting some results.

I also wish to acknowledge the help of Dr Arthur Ernst in the *ab initio* calculations and for his availability for discussions.

Thanks to Dr. Monika Kaempfe for her help in correcting parts of the thesis and for her advice and encouragements in difficult times. Thanks also to my colleagues of the International Max Planck Research School for the friendly atmosphere and for stimulating discussions during the seminars.

Many thanks to Dr. Dirk Sander, Dr. Frank Schumann, Dr. Rodary Guillemin, Dr. Marta Wasnioska, Dr. Zhen Tian, Dr. Zhang Yu, Mr. C-T Chiang, Mr. Sebastien Wedekind for their help.

Sincere thanks to Mrs. Heike Menge, Mr. Herbert Engelhard, Mr. Hartung Detlef, Mr. Frank Helbig for their support.

I also wish to thank the staff of the Mechanical and Electronic workshops for their technical support and the administrative staff for their help and cooperation.

Finally I would like to thank my family for their love and support. To my late mother and brother, I miss you.

Thank you all!!!

Curriculum Vitae

Full name: Achiri Celestine Tange

Date of birth: December 10, 1975

Place of birth: Victoria, Cameroon

Nationality: Cameroonian

Educational History

Sept. 2005-present: PhD candidate at the Max-Planck-Institute of Microstructure
Physics, Halle

Sept. 2002-July 2004: M.Sc. in Physics,
American University in Cairo, Egypt

Sept. 1995-July 1998: B.Sc.(Hons) in Physics,
University of Buea, Cameroon

Professional History

Sept. 1998-June 2002: Math/Physics Teacher and Lab coordinator,
Bishop Rogan College Buea, Cameroon

June 2000-June 2002: Advanced Level Physics Examiner,
Cameroon General Certificate of Education Board

Sept. 2002-June 2005: Teaching/Lab Assistant,
American Univ. in Cairo Physics department.

Halle, Sept. 2008

Achiri C. Tange

Eidesstattliche Erklärung

Ich erkläre hiermit, dass ich keine anderen als die von mir angegebenen Quellen und Hilfsmittel zur Erstellung meiner Dissertation verwendet habe. Den benutzen Werken wörtlich oder inhaltlich entnommene Stellen sind als solche gekennzeichnet.

Achiri C. Tange

Halle (Saale), Sept. 2008